Quadratic Regression Model-Based Indirect Model Predictive Control of AC Drives

Kristóf Bándy and Péter Stumpf

***Abstract*—Model predictive control is a promising technique for electric drives as it enables optimization for multiple parameters and offers reliable operation with nonlinear systems. In this article, a novel approach is presented that aims to harness the advantages of both finite and continuous set model predictive methods in converter-fed ac drive control. The proposed method requires the calculation of only seven predicted states. These states are then assigned cost function values. Using a quadratic regression model, the cost function is mapped to the entire modulation region. After solving a constrained optimization problem on this cost function mapping, the optimal voltage vector is obtained, which is then applied via pulsewidth modulation. The presented method can also be applied to multilevel converter structures without the need to calculate predictions for additional voltage vectors. Therefore, the proposed method does not increase in complexity with the utilized converter topology. Furthermore, the method offers a fixed switching frequency operation and an exact noniterative solution to the optimization problem due to the formulation of the regression model. As a case study, simulation and experimental results verify the operation of the predictive torque control for permanent magnet synchronous machines with the proposed method.**

***Index Terms*—AC machines, multivariable functions, permanent magnet (PM) machines, predictive control.**

I. Introduction

RECENT years have seen an enormous increase in computational power, during which increasingly complex methods were introduced to power electronics. One of these methods is model predictive control (MPC), which chooses the control action based on the predicted state of the controlled device [1]–[4]. Drives controlled by MPC methods have fast dynamic performance and good torque response. Therefore, MPC offers a viable alternative to the widely used field-oriented control (FOC) or direct torque control (DTC), which are considered standard methods in high-performance electric drive control [5].

MPC schemes for power electronic converters and drives can be classified according to several aspects. One aspect is, whether it uses a dedicated modulator or not. If no separate modulator is used, the scheme is direct, and the controller outputs the switching signals directly. In this case, all the applicable voltage vectors of the voltage source inverter (VSI) are evaluated by a cost function to select the optimal control action. In the literature, direct MPC with reference tracking, or in other words finite set MPC (FS-MPC), is the most commonly used method, thanks to its well-known advantages, which are documented in [6]. These include the simple inclusion of nonlinearities and constraints, multivariable control using a single control loop, intuitive design procedure, and a straightforward way of implementation. However, if proper design guidelines are not followed, it can have an inferior performance compared to conventional methods, such as FOC or DTC [2].

One disadvantage of the direct MPC techniques is that they need a high sampling frequency (20–50 kHz) while the typical equivalent switching frequency is around 20%–25% of the sampling frequency [6], [7]. To overcome the problem originating from the low switching frequency, it is not always practical to increase the sampling rate. A multirate MPC algorithm is introduced in [7], where the control frequency is allowed to be faster than the sampling frequency. It allows the switching frequency to be increased without changing the sampling frequency. Another drawback of direct MPC techniques is that the torque ripple can be substantial as only a single voltage vector is applied in each sampling period.

The steady-state performance can be improved by using a so-called implicit modulator stage [1]. In this case, the direct MPC algorithm calculates the switching instant and duty ratios of the voltage vectors applied during one sampling period. The simplest solution is to apply one active and one zero voltage vector and adjust their duty ratios [8], [9]. A so-called generalized multiple-vector-based scheme, which uses two voltage vectors during one sample period, is introduced in [10]. The method has a lower computational burden than conventional methods by utilizing a reference voltage vector obtained from a deadbeat control scheme. An improved version is presented in [11], which uses three voltage vectors during one sampling period. A predictive power control using three voltage vectors with reduced computational complexity is presented in [12] for a doubly-fed induction generator.

Apart from duty ratio regulation, another alternative is to create virtual voltage vectors by discrete space vector modulation. Yang *et al.* [13] presents a two-stage MPC strategy for three-level inverters, which uses 48 virtual voltage vectors. An MPC scheme with 20 applicable voltage vectors is introduced in [14], where

Manuscript received 21 January 2022; revised 6 May 2022; accepted 1 June 2022. Date of publication 10 June 2022; date of current version 26 July 2022. This work was supported in part by the Ministry of Innovation and Technology of Hungary from the National Research, Development and Innovation Fund through Project BME-NVA-02 under Grant TKP2021, in part by the National Research, Development, and Innovation Fund through New National Excellence Program of the Ministry for Innovation and Technology under Grant ÚNKP-22-3-I, and in part by the National Research, Development, and Innovation Office under Grant FK 143429. Recommended for publication by Associate Editor M. Hagiwara. *(Corresponding author: Kristóf Bándy.)*

The authors are with the Department of Automation and Applied Informatics, Budapest University of Technology and Economics, 1111 Budapest, Hungary (e-mail: bandyk@edu.bme.hu; Stumpf@aut.bme.hu).

Color versions of one or more figures in this article are available at https://doi.org/10.1109/TPEL.2022.3181749.

Digital Object Identifier 10.1109/TPEL.2022.3181749

the output voltage vector is innovatively determined through two two-level bang–bang comparators, which reduces the computational time.

Indirect MPC schemes use a normal modulator stage and apply a carrier-based pulsewidth modulation (PWM) scheme. A clear advantage of the indirect MPC scheme is the fixed switching frequency and that the harmonic performance is determined by the applied modulation scheme. One group of these techniques is called explicit MPC, which solves offline for all possible states of the power electronic converter the MPC problem [1]. The design methodology of an explicit MPC using multiparameter quadratic programming (QP) for an ac drive is presented in [15]. These MPC methods have some limitations; therefore, they became less prevalent in practice.

Another form of the indirect MPC scheme that practically ignores the switching nature of power electronic converters is the continuous control set (CCS-MPC). Here an associated QP problem considering the input constraints is solved online [4]. The two most widely used approaches in power electronics applications for QP solvers are the gradient methods [16] and the active-set methods [17]. Cimini *et al.* [17] present an MPC scheme with input and state constraints, where an active-set method is used to solve the QP problem in real time on low-cost hardware. A CCS-MPC method is applied for an ac drive using a special online solver tool called qpOASES in [18]. Ahmed *et al.* [19] compare FS- and CCS-MPC for speed control of induction machines.

The MPC scheme for the control of ac drives can also be classified into two realizations. These are model predictive torque control (MPTC) and model predictive current control (MPCC). MPTC schemes control the torque and the stator flux of the machine similarly to DTC. MPCC algorithms control the real and imaginary components of the stator current, which is similar to FOC. Li *et al.* [20] present a comparative study of FOC and MPC schemes for PMSMs.

This article proposes a novel quadratic regression model-based MPC strategy (QRM-MPC), which evaluates a cost function for seven voltage vectors similarly to direct MPC schemes. Based on the cost function results of the seven voltage vectors, a quadratic regression model is developed that maps the cost function upon the modulation region. After solving a constrained optimization problem, the optimal voltage vector can be applied by a proper PWM scheme, similarly to indirect MPC schemes. In this way, the QRM-MPC can transform an FS-MPC technique into a CCS-MPC approach. Fig. 1 presents a schematic overview of the described concept. In this article, as a case study, the novel strategy is demonstrated for a permanent magnet synchronous machine (PMSM) drive using MPTC; however, it can be utilized in other applications as well.

The theoretical background introducing the applicable voltage vectors and the Tustin approximation-based mathematical modeling of the PMSM is presented in Section II. This is followed by the description of the novel QRM scheme in Section III. As a case study, the proposed algorithm is demonstrated on a PMSM drive. The simulation and experimental results as well as the details of implementation are presented in Section IV.

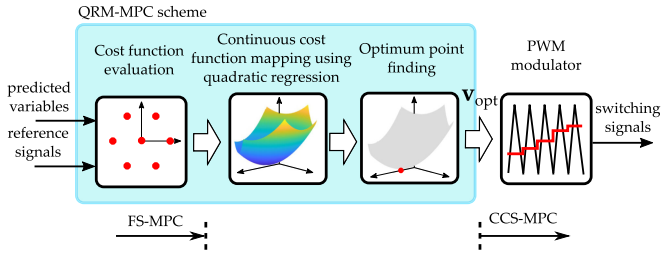

Fig. 1. Schematic representation of the QRM-based control approach. The method receives predictions of the cost of a finite set of control actions and the control reference(s). Then, it maps this finite set to allow the continuous representations of the control actions using regression. The regression establishes the coefficients of a quadratic regression model function. The optimal control action is then determined based on this fit quadratic regression model function.

Section V presents a comparison between the proposed QRM scheme and other techniques available in the literature. Finally, the conclusions can be found in Section VI.

II. Theoretical Background

MPC techniques generally consist of four main steps: measurement and estimation of the state variables, prediction for the selected variables, evaluation of the cost function(s) for the predicted states, and, finally, the selection of the optimal control action. This section summarizes the allowed control options that a VSI can supply. The proposed indirect QRM scheme will be demonstrated on a PMSM drive. As the MPC techniques rely heavily on the mathematical establishment of the controlled system, the discrete model of a PMSM machine is derived in this section by using the Tustin transformation for increased precision.

A. Voltage Vectors of a VSI

Three-phase VSIs, independently of the number of voltage levels, can produce six active voltage vectors in the $\alpha\beta$ stationary reference frame (SRF) ($\mathbf{v}_{\alpha\beta} = [v_\alpha \; v_\beta]^{\mathrm{T}}$) by connecting one or two output phase(s) to the positive dc rail of the inverter while connecting the rest of the phase(s) to the negative dc rail. These voltage vectors have an amplitude of $2/3V_{\mathrm{DC}}$, where V_{DC} is the input dc-link voltage [see voltage vectors in Fig. 2(a) and filled circles in Fig. 2(b) and (c)]. In the case of two-level VSI (2L-VSI), only these active voltage vectors can be generated, while multilevel VSIs (ML-VSI) can generate other active output voltage vectors with smaller amplitudes and different angles as well [see Fig. 2(b) and (c)].

Three-phase VSIs can also produce zero voltage vectors by shorting the output phases. These voltage vectors are redundant and can be realized in different ways. By increasing the number of voltage levels of the VSI, the number of combinations to create zero voltage vector increases as well. Fig. 2(a) presents the zero and active voltage vectors of a 2L-VSI. Fig. 2(b) and (c) shows the achievable voltage vectors for 3 L and 5 L inverters, respectively. The six large voltage vectors and the zero voltage vector, which are utilized during the QRM-MPC approach, are denoted by filled circles in these figures. In the case of ML-VSI,

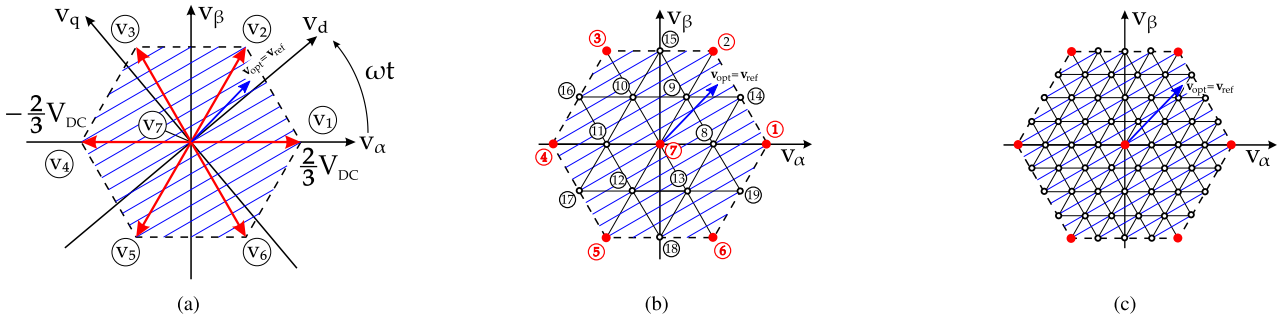

Fig. 2. Available voltage vectors of VSIs. The two-level case [see Fig. 2(a)] can be taken as a general representation for the purposes of this article as only the zero and the large voltage vectors are taken into account when calculating the QRM method regardless of the number of voltage levels. Filled circles denoted these same zero and largest voltage vectors in Fig. 2(b) and (c) for 3 L and 5L-VSIs, respectively. The hatched area represents the modulation region. The main focus of this article is the calculation of the optimal voltage vector. (a) Voltage vectors of a 2L-VSI. (b) Voltage vectors of a 3L-VSI. (c) Voltage vectors of a 5L-VSI.

different types of inverter topologies can be utilized, such as CHB, flying capacitor converter, diode clamped inverter, T-type inverter, or hybrid multilevel inverter. While the topologies are different, with their respective advantages and disadvantages, they can produce the same number of voltage levels and the same output voltage vectors.

The projection of the voltage vectors $\mathbf{v}_1, \ldots, \mathbf{v}_7$ given in Fig. 2(a) in the stationary $\alpha\beta$ complex plane to the dq rotating reference frame (RRF) provides the $\mathbf{v}_{dq} = [v_d\ v_q]^{\mathrm{T}}$ output voltage values. The RRF rotates with the ω_1 synchronous angular speed

$$\underbrace{\begin{bmatrix} v_d \\ v_q \end{bmatrix}}_{\mathbf{v}_{dq}} = \underbrace{\begin{bmatrix} \cos(\omega_1 t) & \sin(\omega_1 t) \\ -\sin(\omega_1 t) & \cos(\omega_1 t) \end{bmatrix}}_{\mathbf{R}(\omega_1 t)} \underbrace{\begin{bmatrix} v_\alpha \\ v_\beta \end{bmatrix}}_{\mathbf{v}_{\alpha\beta}}. \tag{1}$$

In summary, a zero voltage vector and at least six active voltage vectors can be realized by 2L-VSI as well as ML-VSI topologies. Therefore, as it will be presented in Section III, the novel quadratic regression model uses the predictions calculated for these seven voltage vectors since they can be realized by any VSI topology. As it will be demonstrated, the technique works properly, with proper modulation technique, not only for 2L-VSI but also for ML-VSI with an arbitrary number of voltage levels without resulting in any additional computational load in the QRM-MPC algorithm.

B. Discrete Mathematical Model of the PMSM

The equation of a PMSM for both isotropic and anisotropic rotors can be written in the dq RRF. The electrical equations are

$$v_d = R_s i_d + L_d \frac{di_d}{dt} - L_q \omega_1 i_q \tag{2}$$

$$v_q = R_s i_q + L_q \frac{di_q}{dt} + L_d \omega_1 i_d + \Psi_{\mathrm{PM}} \omega_1 \tag{3}$$

where v_d and v_q are the d- and q- axis voltage components, R_s is the stator resistance, L_d and L_q are the d- and q-axis inductance, Ψ_{PM} is the amplitude of the flux induced by the permanent magnets of the rotor in the stator phases. For simplicity, these parameters were assumed constant. Furthermore, $\omega_1 = P\Omega$ is the synchronous angular frequency, where P is the number of pole pairs and Ω is the mechanical speed of the machine. When utilizing a VSI to feed an electric drive, then the control options are the voltage vectors ($\mathbf{v}_{dq} = [v_d\ v_q]^{\mathrm{T}} \in V$) in RRF that the VSI can produce.

The electric torque M of the machine can be given as

$$M = \frac{3}{2} P \Big(\Psi_{\mathrm{PM}} i_q + (L_d - L_q) i_d i_q \Big). \tag{4}$$

In modern high-performance closed-loop drive systems, all the signal processing tasks and control calculations are implemented in the digital domain. Therefore, the continuous-time-domain differential equations shown in this section are to be discretized. The applied discretization technique can have a great impact on the performance; therefore, the selection of the approximation method plays a crucial role.

In this article, to obtain a more accurate prediction of the currents, the so-called trapezoidal (Tustin) integral approximation was used. Although this method increases the computational complexity when compared to the widely used Euler approximation, it is not a gravely limiting factor, as processors with floating-point arithmetic can be purchased at low costs. Furthermore, more stable performance is expected as the Tustin or bilinear approximation provides the best frequency-domain match between the continuous and discretized systems for first-order approximations [21].

According to the Tustin definition, the integral of the d-axis current can be approximated as

$$\int_{kT_s}^{kT_s+T_s} i_d(\tau) d\tau = \frac{\tan(\frac{\omega_0 T_s}{2})}{\omega_0} \Big(i_d(kT_s) + i_d(kT_s + T_s) \Big) \tag{5}$$

where T_s is the sampling time. This also takes into account the so-called prewarping effect caused by the bilinear transform with $\gamma = \tan(\omega_0 T_s/2)/\omega_0$. This effect can be eliminated at one given frequency, which is ω_0. This frequency is set to be equal to the synchronous speed of the machine, $\omega_0 = \omega_1$. The q-axis current can be approximated identically to (5).

The d- and q-axes voltage, as well as the mechanical speed, can be assumed to be constant during one sampling period. Therefore, the d- and q-axes currents can be obtained by

expressing the derivatives of i_d and i_q from (2) and (3) and using (5)

$$i_d(kT_s+T_s) = Ai_d(kT_s) + B\Big(i_q(kT_s+T_s) + i_q(kT_s)\Big) + Fv_d(kT_s) \quad (6)$$

$$i_q(kT_s+T_s) = C\Big(i_d(kT_s+T_s) + i_d(kT_s)\Big) + Di_q(kT_s) + E\Psi_{\text{PM}} + Gv_q(kT_s) \quad (7)$$

where

$$A = 1 - \frac{2R_s}{R_s+\gamma L_d} \quad B = \frac{L_q\omega_1(kT_s)}{R_s+\gamma L_d}$$
$$C = -\frac{L_d\omega_1(kT_s)}{R_s+\gamma L_q} \quad D = 1 - \frac{2R_s}{R_s+\gamma L_q}$$
$$E = -\frac{2\omega_1(kT_s)}{R_s+\gamma L_q} \quad F = \frac{2}{R_s+\gamma L_q} \quad G = \frac{2}{R_s+\gamma L_d}. \quad (8)$$

From (6) and (7), $i_d(kT_s+T_s)$ and $i_q(kT_s+T_s)$ can be expressed in the following matrix form using the notation $\mathbf{i}(kT_s) = [i_d(kT_s)\ i_q(kT_s)]^T$ and $\mathbf{v}(kT_s) = [v_d(kT_s)\ v_q(kT_s)]^T$:

$$\mathbf{i}_{dq}(kT_s+T_s) = \frac{1}{1-BC}\left(\begin{bmatrix} BC+A & B(D+1) \\ C(A+1) & BC+D \end{bmatrix}\mathbf{i}_{dq}(kT_s) + \begin{bmatrix} F & BG \\ CF & G \end{bmatrix}\mathbf{v}_{dq}(kT_s) + \begin{bmatrix} BE \\ E \end{bmatrix}\Psi_{\text{PM}}\right). \quad (9)$$

The electromagnetic torque can be predicted as

$$M(kT_s+T_s) = \frac{3}{2}p\Big(\Psi_{PM}i_q(kT_s+T_s) + (L_d-L_q)i_d(kT_s+T_s)i_q(kT_s+T_s)\Big). \quad (10)$$

III. Quadratic Regression Model Based MPC Scheme

The main contribution of this article is the introduction of a novel quadratic regression model-based indirect MPC control scheme. This control approach uses a finite set of control actions to provide a continuous representation of the control space. The transition from a finite to a continuous set problem is being done via regression. This can be observed in Fig. 1, while a block diagram of the QRM scheme can be seen in Fig. 3 for ac machine drives. This section presents the method with the necessary mathematical background in more detail. The method will be applied and demonstrated on a PMSM drive in this article, but it can be applied to the control of grid-side converters and other types of electrical drives, based on the guidelines presented in this section. The QRM method consists of four steps (*Step 1–Step 4*) to determine the optimal control action. An additional step to gather the required measurement data is also necessary (*Step 0*). Furthermore, an external modulator is also required to generate the switching signals to tailor the calculated optimal voltage vector (*Step 5*). It should be noted that the method is implicit; therefore, these steps have to be calculated for all sampling instants.

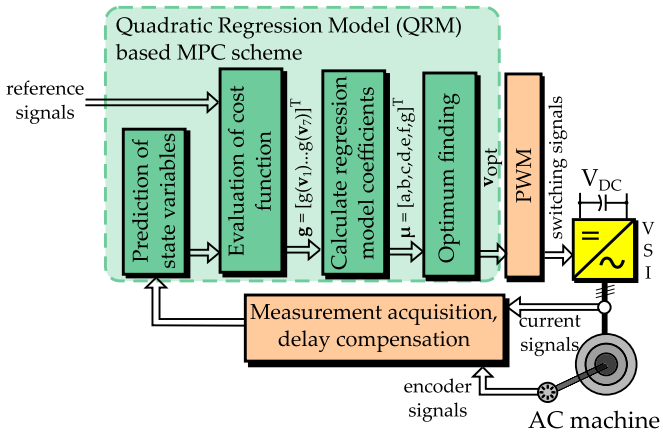

Fig. 3. Block diagram of the QRM-based MPC scheme for ac machine drives.

A. Step 0: Measurement Elaboration and Delay Compensation

This step is not a part of the proposed QRM scheme, but naturally, for any closed-loop control, it has a crucial role in achieving a proper operation. Some state variables, such as phase currents, voltages, or encoder signals of the ac machine, should be measured either because these state variables are directly used or they can be used to estimate state variables, such as the stator flux, which cannot be measured directly. The measured signals are generally valid in the SRF. If it is necessary, such as in the PMSM drive used as a case study in this article, the state variables should be transformed in the RRF in this step.

One well-known disadvantage of the real-time digital implementation of MPC techniques is the required high processing capability due to the excessive number of calculations. It results in a delay between the measurements and the actuation, which can deteriorate the performance of the drive. To overcome the issue caused by this delay, a model-based compensation method is suggested to be used in [6]. The principle of this method is that by using the measured value in the kT_s period, the state variables are estimated by knowing the actual voltage vector for the $kT_s + T_s$ period. In the prediction step (see *Step 2*), the state variables are predicted for the $kT_s + 2T_s$ period.

B. Step 1: Prediction of state variables

Similar to classic FS-MPC schemes, the first step is the prediction of the state variables for different achievable voltage vectors. In the case of the proposed QRM method, the predictions should be evaluated only for six active ($\mathbf{v}_1, \mathbf{v}_2, \ldots, \mathbf{v}_6$) and for one zero voltage vector ($\mathbf{v}_7$) (see Fig. 2), which can be realized both by 2L-VSI as well as ML-VSI. The calculation of the prediction only for seven voltage vectors even for ML-VSI is a clear advantage of the method as the computational load of the predictions can drastically grow by increasing the number of voltage levels of the applied VSI topology.

C. Step 2: Evaluation of the Cost Function

The next step of the introduced method is the calculation of the cost function. The cost function values corresponding to the respective seven voltage vectors are collected in $\mathbf{g} = [g(\mathbf{v}_1) \dots g(\mathbf{v}_7)]^{\mathrm{T}} \in \mathbb{R}^{7\mathrm{x}1}$. The only restriction regarding the cost function in the case of the proposed QRM scheme is that the cost function should contain most quadratic terms. This is true for most of the cost functions used for power electronics applications [22] and agrees with the design guideline presented in [2] that suggests the use of the Euclidean (or l_2) norm to determine the cost of a voltage vector.

D. Step 3: Development of the Quadratic Regression Model for the Continuous Mapping of the Cost Function

The main concept of the method is to develop a continuous quadratic regression model of the cost function in the entire modulation region (see the hatched area in Fig. 2). It is achieved by using the seven discrete cost function values calculated for the six active and one zero voltage vectors. As it will be demonstrated, the established quadratic regression model can perfectly map the cost function on the entire modulation region. By calculating the minimum of the continuous quadratic regression model, where the cost function has the lowest value, the optimal output voltage vector can be determined, which can be formed by proper PWM technique, such as in CCS-MPC techniques. It should be noted this optimization is exact and simple to solve and does not require any iteration, such as other methods in the literature.

For the continuous mapping of the cost function, a multivariable quadratic regression model $m(v_x, v_y, \boldsymbol{\mu})$ is being used. This model is defined as

$$m(v_x, v_y, \boldsymbol{\mu}) = a v_x^2 + b v_x + c v_y^2 + d v_y + e v_x v_y + f \quad (11)$$

where v_x and v_y are V_{DC} independent and normalized voltage vectors, and based in Fig. 2(a), the set of applicable voltage vectors ($\mathbb{V}_{xy}$) is defined as

$$v_x = \frac{3v_\alpha}{2V_{\mathrm{DC}}} \quad v_y = \frac{3v_\beta}{2V_{\mathrm{DC}}}$$
$$\mathbb{V}_{xy} = \left\{ \begin{bmatrix} 1 \\ 0 \end{bmatrix}, \begin{bmatrix} \frac{1}{2} \\ \frac{\sqrt{3}}{2} \end{bmatrix}, \begin{bmatrix} -\frac{1}{2} \\ \frac{\sqrt{3}}{2} \end{bmatrix}, \begin{bmatrix} -1 \\ 0 \end{bmatrix}, \begin{bmatrix} -\frac{1}{2} \\ -\frac{\sqrt{3}}{2} \end{bmatrix}, \begin{bmatrix} \frac{1}{2} \\ -\frac{\sqrt{3}}{2} \end{bmatrix}, \begin{bmatrix} 0 \\ 0 \end{bmatrix} \right\} \quad (12)$$

and $\boldsymbol{\mu} \in \mathbb{R}^{6\mathrm{x}1}$ is the vector of the quadratic regression model coefficients

$$\boldsymbol{\mu} = [a, b, c, d, e, f]^{\mathrm{T}} \quad (13)$$

As it can be seen, the voltage vectors are assumed to be in the stationary $\alpha\beta$ complex plane. Even if the predictions are done in the dq RRF, they can be associated with the exact voltage vector coordinates on the introduced stationary xy normalized plane. Thus, there is no need for an extra coordinate transformation. The vector of the quadratic regression model coefficients $\boldsymbol{\mu}$ can be calculated to fit the cost function values of the seven voltage vectors as

$$\mathbf{g} = \mathbf{X}\boldsymbol{\mu} + \boldsymbol{\varepsilon} \quad (14)$$

where $\mathbf{X} \in \mathbb{R}^{7\mathrm{x}6}$ is the design matrix, which is defined in correspondence with the quadratic regression model

$$\mathbf{X} = \begin{bmatrix} v_{1x}^2 & v_{1x} & v_{1y}^2 & v_{1y} & v_{1x}v_{1y} & 1 \\ v_{2x}^2 & v_{2x} & v_{2y}^2 & v_{2y} & v_{2x}v_{2y} & 1 \\ \vdots & \vdots & \vdots & \vdots & \vdots & \vdots \\ v_{7x}^2 & v_{7x} & v_{7y}^2 & v_{7y} & v_{7x}v_{7y} & 1 \end{bmatrix} \quad (15)$$

and $\boldsymbol{\varepsilon} \in \mathbb{R}^{7\mathrm{x}1}$ corresponds to the error of the quadratic regression model. In order to minimize $||\boldsymbol{\varepsilon}||$, the ordinary least squares estimation can be used to obtain the coefficients of the quadratic regression model [23]

$$\boldsymbol{\mu} = (\mathbf{X}^{\mathrm{T}}\mathbf{X})^{-1}\mathbf{X}^{\mathrm{T}}\mathbf{g}. \quad (16)$$

Since the voltage vectors were taken from the xy normalized SRF, their coordinates will not change during the operation. As always, the same voltage vectors are taken as a basis for the calculations, the design matrix $\mathbf{X}$ will be constant and it can be given as

$$\mathbf{X} = \frac{1}{4}\begin{bmatrix} 4 & 4 & 0 & 0 & 0 & 4 \\ 1 & 2 & 3 & 2\sqrt{3} & \sqrt{3} & 4 \\ 1 & -2 & 3 & 2\sqrt{3} & -\sqrt{3} & 4 \\ 4 & -4 & 0 & 0 & 0 & 4 \\ 1 & -2 & 3 & -2\sqrt{3} & \sqrt{3} & 4 \\ 1 & 2 & 3 & -2\sqrt{3} & -\sqrt{3} & 4 \\ 0 & 0 & 0 & 0 & 0 & 4 \end{bmatrix}. \quad (17)$$

Furthermore, as $\mathbf{X}$ is constant, the matrix $\mathbf{Z} = (\mathbf{X}^{\mathrm{T}}\mathbf{X})^{-1}\mathbf{X}^{\mathrm{T}}$ can be precalculated and only its elements should be stored in the digital controller. According to [24], the matrix $\mathbf{X}^{\mathrm{T}}\mathbf{X}$ is invertible if the chosen voltage vectors are distinct, which is true for the presented case. The coefficient vector $\boldsymbol{\mu}$ can be calculated as

$$\underbrace{\begin{bmatrix} a \\ b \\ c \\ d \\ e \\ f \end{bmatrix}}_{\boldsymbol{\mu}} = \underbrace{\frac{1}{6}\begin{bmatrix} 3 & 0 & 0 & 3 & 0 & 0 & -6 \\ 2 & 1 & -1 & -2 & -1 & 1 & 0 \\ -1 & 2 & 2 & -1 & 2 & 2 & -6 \\ 0 & \sqrt{3} & \sqrt{3} & 0 & -\sqrt{3} & -\sqrt{3} & 0 \\ 0 & 2\sqrt{3} & -2\sqrt{3} & 0 & 2\sqrt{3} & -2\sqrt{3} & 0 \\ 0 & 0 & 0 & 0 & 0 & 0 & 6 \end{bmatrix}}_{\mathbf{Z}=(\mathbf{X}^{\mathrm{T}}\mathbf{X})^{-1}\mathbf{X}^{\mathrm{T}}.} \underbrace{\begin{bmatrix} g(\mathbf{v}_1) \\ g(\mathbf{v}_2) \\ g(\mathbf{v}_3) \\ g(\mathbf{v}_4) \\ g(\mathbf{v}_5) \\ g(\mathbf{v}_6) \\ g(\mathbf{v}_7) \end{bmatrix}}_{\mathbf{g}} \quad (18)$$

The $\boldsymbol{\mu} = \mathbf{Z}\mathbf{g}$ can be calculated with only 8 multiplications and 19 additions due to the favorable form of the matrix $\mathbf{Z}$. The favorable form means here that there are many equal elements in the rows. This can be attributed to the symmetric choice of the voltage vectors. It should be noted that the upper bound for the number of additions and multiplications for an $\mathbb{R}^{6x7}$ matrix is 35 and 42, respectively.

E. Step 4: Optimum Finding

In MPC methods, the controller selects the control action that minimizes the cost function. Since the quadratic regression

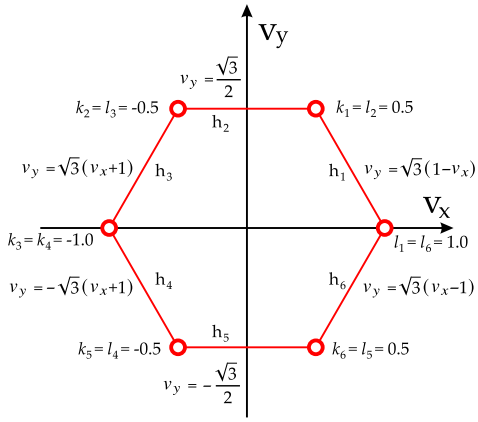

Fig. 4. Visualization of the optimization constraints. The modulation region is bound by the h_i lines that constitute a hexagonal area. The vertices of this region are k_i and l_i points with respect to the v_x coordinate.

model maps the cost function on the modulation region, the minimization problem can be solved on this function. In this way, the optimization is decoupled from the model of the plant, and thus, from (9) and (10), and is only dependent on the quadratic regression model coefficients $\boldsymbol{\mu}$. Since the established quadratic regression model is quadratic and the modulation region is bounded by linear constraints, the optimization problem can be simplified, which is described in detail in this step. Therefore, by using the QRM scheme, the following optimization problem is to be solved:

$$\begin{aligned} &\underset{\mathbf{v}=[v_x,v_y]^{\mathrm{T}}\in\mathbb{R}^2}{\text{minimize}} && m(v_x, v_y, \boldsymbol{\mu}) \\ &\text{subject to} && h_i(v_x, v_y) \leq 0 \text{ for } i = \{1, 2, \ldots, 6\} \end{aligned} \tag{19}$$

where the constraints are defined as the boundary of the modulation region (see Fig. 4)

$$\begin{aligned} h_1(v_x, v_y) &= v_y + \sqrt{3}v_x - \sqrt{3} \\ h_2(v_x, v_y) &= 2v_y - \sqrt{3} \\ h_3(v_x, v_y) &= v_y - \sqrt{3}v_x - \sqrt{3} \\ h_4(v_x, v_y) &= -v_y - \sqrt{3}v_x - \sqrt{3} \\ h_5(v_x, v_y) &= -2v_y - \sqrt{3} \\ h_6(v_x, v_y) &= -v_y + \sqrt{3}v_x - \sqrt{3}. \end{aligned} \tag{20}$$

Since the constraints $h_1, h_2, \ldots h_6$ represent a closed and bounded set and $m(v_x, v_y, \boldsymbol{\mu})$ was defined as a continuous function in (11), therefore based on the Weierstrass extreme value theorem, the function attains a minimum in this compact set.

There are various QP approaches to solve this optimization problem with multiple inequality constraints. These approaches usually assume that the optimum does not violate any of the constraints. This unconstrained optimum is then compared to the

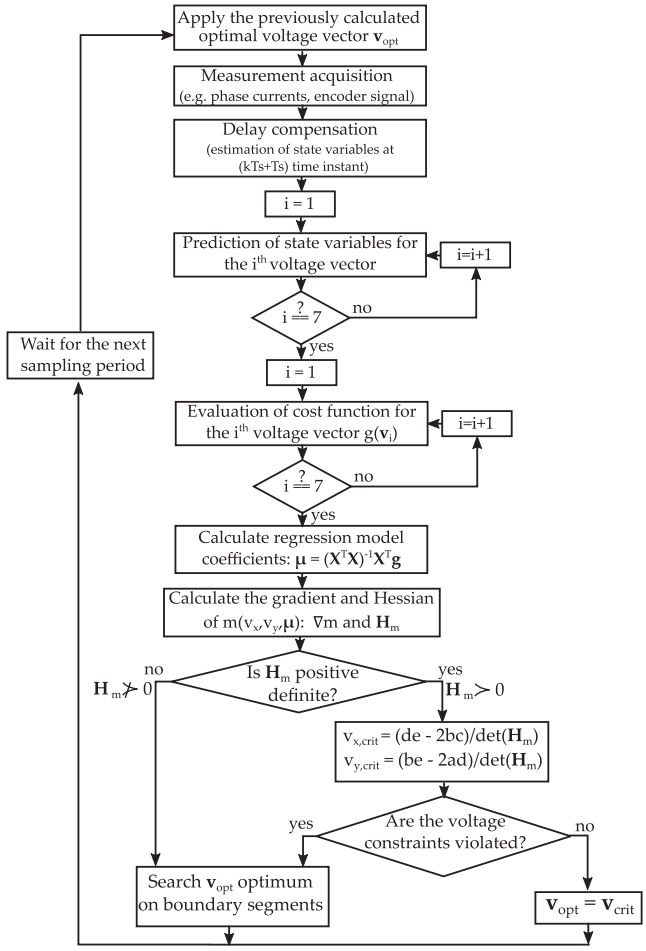

Fig. 5. Flow diagram of the QRM-MPC scheme.

constraints. Should the unconstrained optimum violate any constraints, then the constrained optimum could be found via the Lagrangian multiplier method by taking $h_i(v_x, v_y)$ as equality constraints. However, the quadratic regression model $m(v_x, v_y, \boldsymbol{\mu})$ and the linear constraints allow some simplifications, as detailed in the following. Fig. 5 summarizes the steps of the devised MPC method and the optimum finding algorithm, which is described as follows.

1) Calculating the Unconstrained Optimum: The proposed quadratic regression model $m(v_x, v_y, \boldsymbol{\mu})$ is a second-degree polynomial function, which only has one critical point. This point can be found using the gradient vector, and via the Hessian matrix, it can be determined whether it is a minimum, maximum, or saddle point (this can be seen later in Fig. 6). The gradient and the Hessian can always be calculated since polynomial functions are continuously differentiable. The gradient and Hessian of $m(v_x, v_y, \boldsymbol{\mu})$ are, respectively

$$\nabla m(v_x, v_y, \boldsymbol{\mu}) = \begin{bmatrix} 2av_x + b + ev_y \\ 2cv_y + d + ev_x \end{bmatrix} \quad \mathbf{H}_m = \begin{bmatrix} 2a & e \\ e & 2c \end{bmatrix}. \tag{21}$$

Note that $\mathbf{H}_m$ is only dependent on the quadratic regression model coefficients. If the critical point is a minimum, then the respective Hessian $\mathbf{H}_m$ matrix is positive definite ($\mathbf{H}_m \succ 0$),

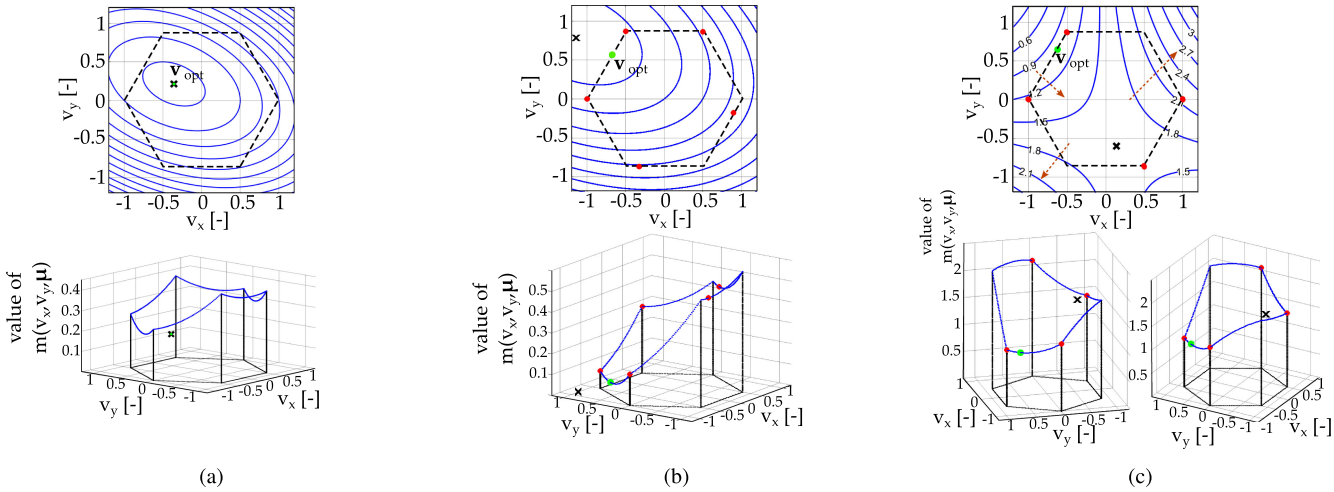

Fig. 6. Example cases for the optimum finding. The cross marks the critical point based on the gradient criterion given in (23). The upper figures represent the contour plots for each of the cases, while the lower figures represent the cost function on the boundary. In the cases of (b) and (c), all boundary optima are marked and the constrained optimum is the minimum of this set of values. (a) Minimum inside the boundary constraints (unconstrained optimum), where μ =[0.10, 0.05, 0.20, −0.05, 0.10, 0.20]$^{\mathrm{T}}$. (b) Minimum outside the boundary constraints (constrained optimum), where μ =[0.10, 0.15, 0.20, −0.20, 0.10, 0.20]$^{\mathrm{T}}$. (c) Saddle point example, optimum is on the boundary (constrained optimum), where μ =[0.10, 0.45, 0.05, −0.05, 0.80, 1.60]$^{\mathrm{T}}$.

which can be decided in this case by checking if both principal minors are positive

$$H_{m,11} = 2a > 0$$
$$\det(\mathbf{H}_m) = 4ac - e^2 > 0. \tag{22}$$

The critical point can be found by solving the $\nabla m(v_x, v_y, \boldsymbol{\mu}) = \mathbf{0}$ equation system, which yields

$$\mathbf{v}_{\text{crit}} = \begin{bmatrix} v_{x,\text{crit}} \\ v_{y,\text{crit}} \end{bmatrix} = \frac{1}{4ac - e^2} \begin{bmatrix} de - 2bc \\ be - 2ad \end{bmatrix}. \tag{23}$$

If $\mathbf{H}_m \succ 0$, then based on (23), the unconstrained optimal voltage vector can be determined. This unconstrained optimum is accepted as the optimal voltage vector if and only if the constraint inequalities in (20) are all satisfied. In this case, the unconstrained optimum is accepted as the optimum $\mathbf{v}_{\text{opt}} = \mathbf{v}_{\text{crit}}$, and the results are forwarded to the modulator. As an illustrative example, Fig. 6(a) presents a contour plot as well as the three-dimensional plot of a quadratic function along the boundary of the hexagon, where $\mathbf{v}_{\text{opt}} = \mathbf{v}_{\text{crit}}$ is a minimum and it is inside the boundary constraints.

2) Calculating the Constrained Optimum: If $\mathbf{H}_m \not\succ 0$, based on (22), or the unconstrained optimum violated any of the constraints of (20), then the optimum can be found on the boundary of the set based on the extreme value theorem. The boundary consists of six linear constraints $h_i(v_x, v_y)$, which also restrict each other. For example, the h_2 constraint is bounded by h_1 and h_3. Therefore, the constrained optimum can be found via the calculation of six constrained optimization problems that are restricted for the h_i linear boundaries

$$\begin{aligned} \underset{\mathbf{v}=[v_x,v_y]^{\mathrm{T}}\in\mathbb{R}^2}{\text{minimize}} \quad & m(v_x, v_y, \boldsymbol{\mu}) \\ \text{subject to} \quad & h_i(v_x, v_y) = 0 \text{ for } i = \{1, 2, \ldots, 6\} \\ & v_x \geq k_i \text{ for } i = \{1, 2, \ldots, 6\} \\ & v_x \leq l_i \text{ for } i = \{1, 2, \ldots, 6\} \end{aligned} \tag{24}$$

where k_i and l_i represent the interaction of two neighboring constraints. Since h_i is an equality constraint, it allows the calculation of the v_y coordinate as a function of v_x. Therefore, it is enough to constrain the v_x variable to inequality constraints. It is important to note that the QP problem presented in (24) represents six individual optimization problems, with only the ith constraints active for each

$$\begin{aligned} k_1 &= 0.5l_1 = 1.0 \\ k_2 &= -0.5l_2 = 0.5 \\ k_3 &= -1.0l_3 = -0.5 \\ k_4 &= -1.0l_4 = -0.5 \\ k_5 &= -0.5l_5 = 0.5 \\ k_6 &= 0.5l_6 = 1.0. \end{aligned} \tag{25}$$

Using the Lagrangian multiplier method, the solution would be to calculate the unconstrained optima for each of the bounds and reintroduce the k_i or l_i constraints, if necessary. However, the method presented in this article to calculate this constrained optimization problem leverages the properties of the quadratic regression model $m(v_x, v_y, \boldsymbol{\mu})$ and the constraining equations. It can be observed that the $h_i(v_x, v_y)$ are now equality constraints such that the v_y variable can be expressed. The constrained quadratic regression model for a given h_i constraint is, thus, denoted with $m_i(v_x, \boldsymbol{\mu})$, with the quadratic regression model

simplified to a function with v_x as the single independent variable. These constrained quadratic regression model functions are listed in Appendix A in (28). The resulting function retains its quadratic form in this process. Therefore, the optimum for a boundary segment can be found via the first and second derivatives of $m_i(v_x, \boldsymbol{\mu})$ with respect to v_x. Since the optimization problem remains the same for all sampling time, these derivatives can be precalculated such that the digital controller only has to substitute the coefficients contained in $\boldsymbol{\mu}$ to obtain the optimum.

The critical point for the ith boundary segment $v_{x,i,\text{crit}}$ can be found via the first derivative and is only dependent on the coefficients of the quadratic regression model. The calculation of the critical point for each of the boundary segments is included in Appendix A in (29). The second derivatives decide whether the critical point is a minimum or a maximum. These are all constant and only depend on the coefficients of the quadratic regression model. The calculation of the second derivatives is given in Appendix A in (30).

However, this calculation only results in an unconstrained optimum for all of the line segments. However, due to the quadratic regression model being a second-degree polynomial, the constrained optimum can be obtained simply from the critical point $v_{x,i,\text{crit}}$ and the sign of the second derivative of $m_i(v_x, \boldsymbol{\mu})$. The entire calculation for the constrained optimum on a boundary segment is presented with Algorithm 1. During the algorithm, if the critical point turned out to be a maximum, then the minimum of the constrained function at the endpoint of the interval be $[k_i, l_i]$, which is farther from the critical point. This is due to the symmetry of the quadratic functions. Thus, the position of the critical point and the arithmetic mean of k_i and l_i are established (M variable).

In Algorithm 1, the optimum for all boundary segments is established as $m_{i,\text{opt}}$ for each of the constrained optima $v_{x,i,\text{crit}}$. The $v_{y,i,\text{crit}}$ coordinate can be established with the respective $h_i(v_x, v_y) = 0$ equality constraint. Therefore, the constrained optimum that satisfies the primary QP problem (19) is

$$\mathbf{v}_{\text{opt}} = \underset{i\in\{1,2,\ldots,6\}}{\arg\min}\ m(v_{x,i,\text{crit}}, v_{y,i,\text{crit}}, \boldsymbol{\mu}). \tag{26}$$

Fig. 6(b) and (c) presents a contour plot as well as the three-dimensional plot of the quadratic function along the boundary of the hexagon for demonstration purposes. In Fig. 6(b), the calculated critical point is a minimum, but it can be found outside the modulation region. Fig. 6(c) presents a case, where $\mathbf{v}_{\text{crit}}$ can be found within the boundary, but it is a saddle point; therefore, the minimum point should be searched on the boundary line segments. As it can be seen in the lower diagrams of Fig. 6(c), a local maximum point can be found on one of the line segments. In both Fig. 6(b) and (c), the optimum points for each of the boundary segments are marked.

3) Remark on the Computational Complexity: It should be noted that the number of mathematical operations—either for constrained or unconstrained optimum—is fixed, which is a great advantage of the method over other techniques, which use iterative methods to find the optimal point [17], [25], [26]. Table I contains the required arithmetic operations for all the above-mentioned steps. The computational cost of the quadratic regression model fitting and the proposed QP solution in the worst case—$\mathbf{H}_m \succ 0$ and Constrained Optimum—is 119 multiplications, 73 additions, and 4 divisions (see Table I, the sum of Steps 3 and 4). Furthermore, the number of calculations does not increase if the number of voltage levels is increased, which is also a unique advantage of the proposed scheme.

To demonstrate that the number of mathematical operations of the QP solution is not so much, let us consider an illustrative example: let us assume a PMSM drive supplied by a three-level VSI. In the case of the classic FS-MPC approach, the state

Algorithm 1: Boundary Optima Calculation.

```
i ← 1
while i < 7 do
  v_{x,i,crit} ← (29).i
  m_{xx,i} ← (30).i
  if m_{xx,i} ≥ 0 then                    ▷ v_{x,i,crit} is a minimum
    if v_{x,i,crit} < k_i then
      v_{x,i,crit} = k_i
    else if v_{x,i,crit} > l_i then
      v_{x,i,crit} = l_i
    end if
  else                                    ▷ v_{x,i,crit} is a maximum
    M ← k_i + l_i
    M ← 0.5 · M
    if v_{x,i,crit} < M then
      v_{x,i,crit} = l_i
    else
      v_{x,i,crit} = k_i
    end if
  end if
  m_{i,opt} ← m_i(v_{x,i,crit}, μ)
  i ← i + 1
end while
```

TABLE I
NUMBER OF ARITHMETIC OPERATIONS OF THE QRM SCHEME AT DIFFERENT STEPS

Phase	Number of		
	multiplication	addition	division
Step 1[1,2] Step2	112	70	0
Step 3	8	19	0
Step 4: calculate $\det(\mathbf{H}_m)$	3	1	0
Step 4: Unconst. Optimum	8	2	1
Step 4: Const. Opt. $\mathbf{H}_m \not\succ 0$	103	52	3
Step 4: Const. Opt. $\mathbf{H}_m \succ 0$	111	54	4
Total number of operation for worst case	234	144	4

[1] The number of the arithmetic operations also depends on the used discrete model of the ac machine. The number of operations is given for the derived Tustin model of the PMSM introduced in Section II-B.
[2] The number of arithmetic operations for the calculation of the $A, B, \ldots, G$ parameters used in the prediction equations is not included.

variables should be predicted and the cost function should be calculated for all the 19 possible voltage vectors. By using the proposed QRM scheme, it is enough to carry out the predictions and the cost function evaluation only for seven voltage vectors. The operations required for the "extra" 12 voltage vectors are 192 multiplications and 120 additions by using the Tustin discrete model presented in Section II-B. This calculation of FS-MPC for a three-level inverter requires much more time than the presented optimum finding algorithm with the calculation of the quadratic regression model coefficients even if there are division(s) in the proposed method.

TABLE II
PMSM PARAMETERS

Symbol	Description	Value	
P_n	Rated output power	70	W
n_n	Rated speed	2800	r/min
P	No. of pole pairs	5	
R_s	Phase resistance	0.285	Ω
L_d	d-axis inductance	0.32	mH
L_q	q-axis inductance	0.32	mH
Ψ_{PM}	Flux of PM	0.0079	Wb
$\lvert \mathrm{M}_{\max} \rvert$	Maximum reference torque	0.25	N·m

F. Step 5: Modulation

After the fourth step of the proposed QRM approach, an optimal voltage vector $\mathbf{v}_{\mathrm{opt}}$ in the stationary complex xy normalized plane is obtained. As an additional step, this voltage vector, which acts as a reference voltage vector $\mathbf{v}_{\mathrm{ref}} = \mathbf{v}_{\mathrm{opt}}$ [see voltage vectors in Fig. 2(a)–(c)] for the dc/ac conversion, should be generated by the VSI by using a proper PWM technique. The modulation technique is not directly part of the QRM scheme as it was defined as an indirect MPC method. However, since the utilized modulation technique directly affects the performance, some aspects of modulation techniques utilized in VSI topologies are discussed here. The QRM-MPC scheme can be used either for 2L-VSI or ML-VSI as the calculation procedure (see Steps 1-4) does not depend on the applied inverter topology and the number of voltage levels. The cost functions should be evaluated for seven voltage vectors [see $\mathbf{v}_1, \ldots, \mathbf{v}_7$ in Fig. 2(a), and the filled circles in Fig. 2(b) and (c)] to use quadratic regression to continuously map the cost function upon the modulation region. These seven voltage vectors can be realized both by three-phase 2L-VSI and ML-VSI, as it was mentioned in Section II.

PWM techniques can be classified in multiple ways. Space vector modulation (SVM) and carrier-based PWM (CB-PWM) methods are perhaps the two most widely applied modulation schemes either for 2L-VSI and ML-VSI. The main purpose of SVM-based algorithms is to determine the three adjacent voltage vectors, their duty cycles or switching times, and their switching sequence to approximate, in average, the reference voltage vector $\mathbf{v}_{\mathrm{ref}}$ for one switching period [27]. Usually, duty cycles and switching times can be determined by geometry-based calculations by projecting the reference voltage vector over the triangle formed by the closest voltage vectors. For example, in 2L-VSI, the reference voltage vector $\mathbf{v}_{\mathrm{ref}} = \mathbf{v}_{\mathrm{opt}}$ [see Fig. 2(a)] can be formed with the help of the two closest active voltage vectors ($\mathbf{v}_1$ and $\mathbf{v}_2$) and zero voltage vector ($\mathbf{v}_7$) (the latter one is redundant and can be realized in two ways). For example, for a 3L-VSI, the $\mathbf{v}_{\mathrm{ref}} = \mathbf{v}_{\mathrm{opt}}$ reference voltage vector [see Fig. 2(b)] can be formed by the voltage vectors denoted by 2, 9, and 14.

In the case of CB-PWM techniques, sinusoidal reference or modulation signals for each phase are compared with a triangular carrier signal to produce the switching signals. The sinusoidal reference signals can be calculated from $\mathbf{v}_{\mathrm{ref}} = \mathbf{v}_{\mathrm{opt}}$ by using inverse space vector transformation and normalization. The sinusoidal modulation signals can be modified by some zero-sequence component to expand the linear modulation region. By properly selecting the zero-sequence component, the CB-PWM can become completely equivalent to SVM. It should be noted that for 2L-VSI, one common triangular carrier signal is used for each phase, while for ML-VSI topology, more carrier signals are necessary depending on the number of voltage levels. These carrier signals can be either phase-shifted or level-shifted depending on the given inverter topology.

It should also be mentioned that if the amplitude of the resulting optimal voltage vector is larger than $\frac{V_{\mathrm{DC}}}{\sqrt{3}}$, for example, in the close vicinity of the boundary, then the VSI should operate in the so-called overmodulation region. Special care should be paid to the overmodulation region to obtain a proper harmonic performance [28]. In some ML-VSI topologies, for example, the 3 L neutral point clamped (NPC) inverter, it is necessary to balance the voltage across the dc bus capacitors. If the inverter is controlled by MPC approaches, the neutral point balancing is included in the cost function, which suffers from tedious weighting factor selection [29]. By using the proposed QRM scheme, there is no need to include this control objective in the cost function. The voltage balance can be realized by a proper PWM modulation scheme [30].

Naturally, the applied PWM technique, depending on the number of voltage levels and inverter topology, causes an additional computational load. However, as the modulation step is not a part of the QRM scheme, it does not modify the computational complexity of the proposed method. Furthermore, thanks to the well-developed PWM techniques with a low-computational burden introduced in the literature, the calculation time of the modulation step is not crucial. A comprehensive overview of PWM schemes for 2L-VSI and ML-VSI, both for linear and overmodulation regions, can be found in [27], [28], [30], and [31].

IV. CASE STUDY: MPTC OF PMSM USING QRM APPROACH

The developed QRM scheme will be presented on a low-power Hurst DMA0204024B101 PMSM drive using MPTC as a case study. The main parameters of the drive are summarized in Table II. This section presents the block diagram and the operation of the QRM-based MPTC algorithm as well as the simulation and experimental results conducted on this drive.

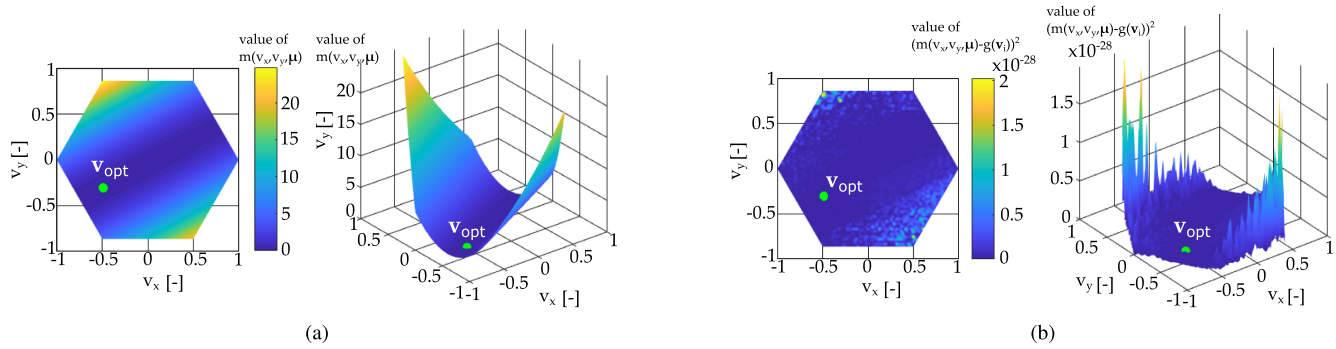

Fig. 7. Block diagram of the PMSM control with QRM-MPTC.

A. MPTC Scheme

The block diagram of the commonly used direct MPTC scheme is shown in Fig. 7, where an external PI speed controller generates the M_{ref} reference value of the electric torque using the difference between the reference (Ω_{ref}) and the measured (Ω) rotational speeds. The proposed indirect QRM-MPTC scheme predicts the d and q axes currents and the electromagnetic torque for seven voltage vectors of the VSI by using (9) and (10).

The MPTC scheme described in this article utilizes two feature costs $\xi_1(\mathbf{v}_i)$ and $\xi_2(\mathbf{v}_i)$. The first feature expresses the torque error, while the second one is the so-called maximum torque per ampere (MTPA) criterion [32]. Their equations as well as the resulting cost function can be given as

$$\begin{aligned} g(\mathbf{v}_i) &= \xi_1(\mathbf{v}_i) + \lambda \xi_2(\mathbf{v}_i) \\ &= \left(M_{\text{ref}} - M(\mathbf{v}_i)\right)^2 + \lambda \left(i_d(\mathbf{v}_i)\right)^2 \end{aligned} \tag{27}$$

where λ denotes the weighting factor.

This article aims to present the concept of the QRM-MPC method in an MPTC scheme. Therefore, a symmetric PMSM drive was selected as a case study for demonstration purposes. The proposed method can be used for other applications as well. As it was mentioned previously, the only constraint is that the cost function should contain terms up to a second degree. For example, the cost feature expressing the MTPA criterion for nonsymmetrical PMSM ($L_d \neq L_q$) given in [32] contains terms up to the fourth degree of both i_d and i_q, and therefore, the quadratic regression model will not be able to perfectly map the cost function in the modulation region. However, by using a modified feature cost having quadratic terms, the method can be applied for nonsymmetrical PMSMs as well.

B. Simulation Results

In order to present the potential of the QRM-MPC algorithm, a complete simulation model was established using a 2L-VSI in MATLAB/Simulink environment. The mathematical model also took into account the computational delay. During the simulation study, ideal switching devices were assumed. The dc-link voltage was $V_{\text{DC}} = 24$ V and the sampling frequency of the MPC algorithm was selected to be $f_s = 1/T_s = 10$ kHz. The external speed control loop ran at a smaller rate at $f_{s,\text{speed}} =$ 1 kHz. The value of the weighting factor [see (27)] was selected to be unity.

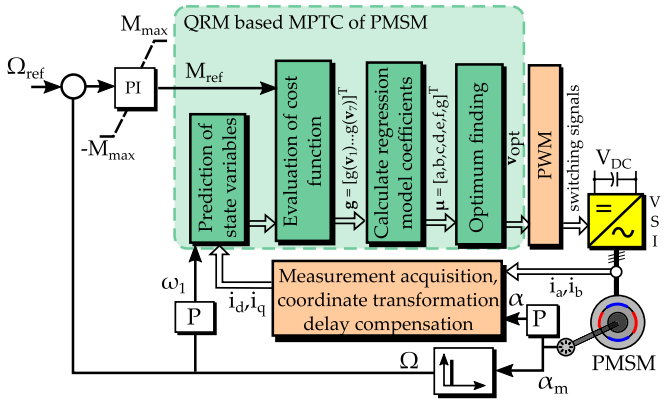

Fig. 8. Visualization of the cost function mapping for the calculation example presented in Appendix C. The mapping in (a) was established using the seven defined voltage vectors, while the square of the residuals between the cost function values of actual and modeled voltage vector predictions is presented in (b) for a large set of voltage vectors. (a) Cost function mapping by the quadratic regression model. (b) Squared cost function residuals between the calculated predictions and the fit quadratic regression model.

1) Model Fitting Results: Since the established quadratic regression model is a linear combination of terms, the coefficient of determination or the R^2 value can be used to measure the goodness-of-fit. Further remarks on the calculation of the R^2 value can be found in Appendix B.

As an illustrative example, Fig. 8(a) presents the cost function mapping in the entire modulation region calculated by the proposed QRM scheme. The calculation steps for the working point presented in Fig. 8(a) are given in Appendix C. As it can be seen for this parameter set, the optimum voltage vector $\mathbf{v}_{\text{opt}}$ can be found inside the modulation region, so it is an unconstrained optimum ($\mathbf{H}_m \succ 0$, no voltage constrained violated), thus the optimum coordinates were calculated by using (23).

In order to validate the proof of concept and to demonstrate that the scheme can be used for ML-VSI as well, the cost function is evaluated at the same working points for all the achievable voltage vectors for a 3L-VSI (see Appendix C). The values are compared with the cost function values calculated from the regression model. Table III contains the results. An important

TABLE III
PREDICTED RESULTS FOR A 2L-VSI WITH THE INCLUSION OF THE 12 ADDITIONAL VOLTAGE VECTORS OF A 3L-VSI AT A GIVEN WORKING POINT

i	$v_{i,x}$ [1]	$v_{i,y}$ [1]	$i_{i,d}(kT_s+2T_s)$ [A]	$i_{i,q}(kT_s+2T_s)$ [A]	$g(\mathbf{v}_i)$ [1]	$m(v_{i,x}, v_{i,y}, \boldsymbol{\mu})$ [1]	residual squares [1]
Voltage vectors of a 2L-VSI							
1	1.00	0.00	−2.0554	−3.8256	4.3954	4.3954	12.622e-30
2	0.50	$0.50\sqrt{3}$	2.7267	−3.6639	7.598	7.5980	7.0997e-30
3	−0.50	$0.50\sqrt{3}$	4.9777	0.5583	24.802	24.802	12.622e-30
4	−1.00	0.00	2.4467	4.6189	5.9939	5.9939	7.0997e-30
5	−0.50	$-0.50\sqrt{3}$	-2.3354	4.4572	5.4601	5.4601	0.0000e-30
6	0.50	$-0.50\sqrt{3}$	-4.5864	0.2350	21.065	21.065	12.622e-30
7	0.00	0.00	0.1957	0.3967	0.0649	0.0649	26.652e-30
Additional voltage vectors of a 3L-VSI							
8	0.50	0.00	-0.9299	−1.7145	0.9477	0.9477	20.720e-30
9	0.25	$0.25\sqrt{3}$	1.4612	−1.6336	2.2154	2.2154	3.1554e-30
10	−0.25	$0.25\sqrt{3}$	2.5867	0.4775	6.7161	6.7161	0.0000e-30
11	−0.50	0.00	1.3212	2.5078	1.7469	1.7469	7.0997e-30
12	−0.25	$-0.25\sqrt{3}$	-1.0699	2.4270	1.1465	1.1465	21.743e-30
13	0.25	$-0.25\sqrt{3}$	-2.1954	0.3158	4.8479	4.8479	19.722e-30
14	0.75	$0.25\sqrt{3}$	0.33567	−3.7447	0.2796	0.2796	1.1124e-30
15	0.00	$0.50\sqrt{3}$	3.8522	−1.5528	14.917	14.917	12.622e-30
16	−0.75	$0.25\sqrt{3}$	3.7122	2.5886	13.782	13.782	0.0000e-30
17	−0.75	$-0.25\sqrt{3}$	0.0556	4.5381	0.0099	0.0099	4.7927e-30
18	0.00	$-0.50\sqrt{3}$	-3.4609	2.3461	11.980	11.980	0.0000e-30
19	0.75	$-0.25\sqrt{3}$	-3.3209	−1.7953	11.114	11.114	12.622e-30

observation is that the squares of the residuals (see Appendix C) are in the range of 10^{-30} for all voltage vectors even if they were not chosen for the establishment of the model. Therefore, it can be concluded that the regression model can practically perfectly map the cost function values for all of the voltage vectors.

Another illustrative example is given in Fig. 8(b) for the same working point. Here, a 32-level inverter was assumed, which can generate theoretically 2977 different voltage vectors with different angles and magnitudes. Naturally, such an inverter is not practical due to its complexity. However, it can be used in theory to validate and demonstrate the effectiveness of the proposed QRM scheme due to a large number of data points. The prediction and cost function calculation was carried out for each of these 2977 voltage vectors by using (9), (10), and (27). The results were compared with the cost function values calculated from the quadratic regression model using (11). For the comparison, squares of the residual values are used, which are calculated as $(g(\mathbf{v}_i) - m(v_{i,x}, v_{i,y}, \boldsymbol{\mu}))^2$ for $i \in [1, 2977]$.

The R^2 values obtained from fitting the quadratic regression model on the working point data were practically 1. This is due to the square sum of residuals ($\text{SS}_{\text{residual}}$) being in the 10^{-27}s order of magnitude and the SS_{total} values being in the 10^3. Since the described quadratic regression model uses six coefficients, therefore the use of the adjusted R-squared or $\overline{R}^2$ value is warranted. However, since R^2 is this extremely close to 1, the value of $\overline{R}^2$ will follow suit. Fig. 8(b) presents the square of the cost function residual mapping for the working point calculated in Appendix C. Based on the results, it can be concluded that the QRM could perfectly predict the cost function value of any voltage vector in the bounds of the system.

Based on the quadratic regression model definition in (11), the model has six coefficients corresponding to the linear and quadratic terms. It is, therefore, necessary to check whether all terms will contain significant information [23]. The coefficients can be tested independently using a two-sample t-test, where one sample is generated with all the coefficients fit on the dataset and the other sample is generated with one coefficient set to zero. The entire quadratic regression model can be tested using the analysis of variance on the fit model. For both tests, all the coefficients got a p-value $p < 0.0001$ at a significance level of $\alpha = 5\%$, thus indicating that all coefficients in the quadratic regression model contain significant information.

Although the previously presented analysis on the model fitting was established only for a single working point, it was observed that the minuscule difference between the value of R^2 and unity [see (39)] was closely retained for both transient and steady-operation in both simulation and experimental tests. Therefore, it can be concluded that the method can practically perfectly map the cost function upon the modulation region. This implies that solving the optimization problem for the quadratic regression model provides the actual optimal control voltage vector.

2) Dynamic Performance: Simulation results using the QRM-MPC scheme are shown in Fig. 9. In this figure, a speed reference step change ($\Omega_{\text{ref}} = -220$ rad/s) was performed at time t = 0.1 s, then a speed reversal at time t = 0.5 s, and finally, a load step ($M_{\text{load}} = 0.2$ N · m) was applied at time 1.1 s. It can be seen from these results that all of the objectives of the control were achieved during the tests. The mechanical speed followed its reference value with a near-zero overshoot. The acceleration rate was only limited by the maximum allowable

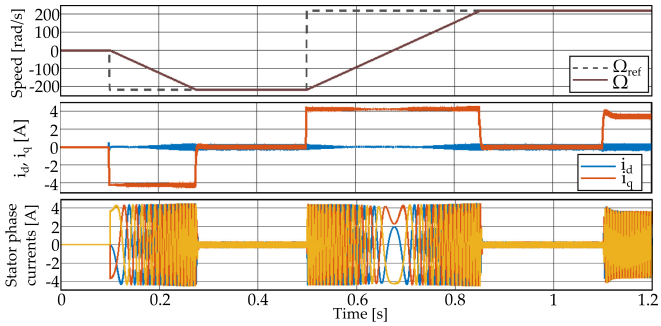

Fig. 9. Simulation results, step response of the method to changes in Ω_{ref} and M_{ref}.

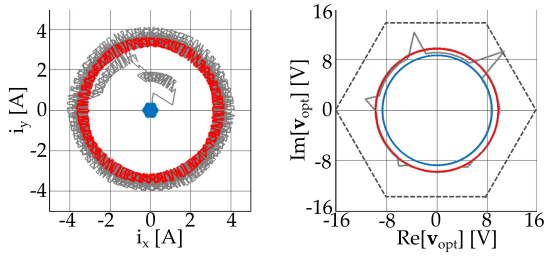

Fig. 10. Current (left) and voltage (right) vector trajectories during the step change of the applied torque. The hexagonal boundary formed by the six active voltage vectors that were used for the calculation of the predicted state is represented by dashed line.

torque. Furthermore, fast-tracking of the torque-producing i_q current was achieved while the d-axis current was zero. Fig. 10 presents the trajectory of the current space vector as well as the calculated optimal voltage vector during the transient caused by the step change in the load torque. In steady state, the path of the optimal voltage vector was a circle similar to FOC.

3) Parameter Sensitivity: In order to test and evaluate the parameter sensitivity of the QRM-MPC scheme, a simulation analysis was carried out. In Fig. 11(a) and (b), the reference speed was selected to be $\Omega_{\text{ref}} = 50$ and $\Omega_{\text{ref}} = 220$ rad/s, respectively. The machine loading torque was changed suddenly in both directions periodically. The values of the stator resistance [see Fig. 11(a)] and the q-axis inductance [see Fig. 11(b)] in the simulated PMSM model were changed abruptly in both directions by 50%, while the QRM-MPC scheme used their nominal values for predictions. As it can be seen, the QRM-MPC scheme is robust against parameter variations. Even such a high difference in the parameters resulted in stable operation with acceptable performance.

4) Application the QRM-MPC Scheme for ML-VSI: As it was mentioned previously, the QRM-MPC scheme can be applied for ML-VSI topologies as well by modifying only the modulation scheme. For demonstration, Fig. 12(b) presents the time function of the i_α real and i_β imaginary components of the stator current vector in SRF as well as the v_α real and v_β imaginary components of the stator voltage also in SRF when the PMSM was supplied by an NPC-type three-level VSI. For simplicity, the potential of the neutral point of the inverter was fixed. The reference speed again was $\Omega_{\text{ref}} = 220$ rad/s and the machine was loaded its rated value ($M_{\text{load}} = 0.2$ N $\cdot$ m). The MPC scheme is the same as for 2L-VSI, only the SVM algorithm is modified accordingly. For a better comparison, Fig. 12(a) presents the same waveforms for 2L-VSI. The voltage and the current signals show the typical waveforms delivered by 2L-VSI and three-level VSI. Naturally, the harmonic distortion is smaller for the latter case. The results demonstrate that the QRM-MPC scheme can be used for ML-VSI topology as well by using a proper modulation scheme.

C. Hardware Implementation

The discrete algorithm of the QRM-MPC scheme was implemented using C language on a low-cost dual-core TM320F28379D DSP running at 200 MHz clock frequency. The implementation utilized only one core; however, a core-independent 32-bit floating-point math accelerator called control law accelerator (CLA) was also used.

During operation, the CPU handles the peripherals, such as timers, ADC, PWM, and QEP units, while the CLA is tasked with the execution of the MPC algorithm completely. The MPTC algorithm is being called by the CPU at a fixed sampling frequency of $f_s = 1/T_s = 10$ kHz using an interrupt routine. Similar to the simulation study, the external speed control loop runs at a smaller sampling rate. The parameters of the measured PMSM are the same as in the simulation study. During the test, a three-phase LMG5200 GaN MOSFET-based inverter was used as the 2L-VSI. The method was also tested by using a three-level CHB inverter using the same GaN MOSFETs. A photo of the laboratory setup can be seen in Fig. 13. In the figure, it can be observed that the controlled and the loading machines are identical.

D. Turnaround Time

Fig. 14 presents the measured turnaround time of the QRM-MPC scheme comparatively with 2L-VSI and 3L-VSI FS MPC schemes. The diagram presents the turnaround time for the unconstrained optimal optimum—with no constraints violated—($t_{\text{TAT}} = 12.14\ \mu$s), and the constrained optimum time—$\mathbf{H}_m \succ 0$, but violated constraints – ($t_{\text{TAT}} = 16.67\ \mu$s). The latter case includes the unconstrained optimum calculations due to the optimization solution; therefore, it can be considered the worst-case operation of the algorithm.

For demonstration purposes, the turnaround times of FS-MPTC by using a 2L-VSI and a 3L-VSI are also presented in Fig. 14. In the first case, the prediction and cost function evaluation was carried out for seven voltage vectors, while for 3L-VSI for 19 voltage vectors. In both cases, after calculating the cost function values for all the possible voltage vectors, the voltage vector that minimizes the cost function was selected.

It can be seen that the QRM-MPC scheme has practically the same turnaround time compared to the classic scheme using 2L-VSI if the optimum can be found in the hexagonal bounds. By comparing with the classic scheme using 3L-VSI, it can be seen the QRM-MPC algorithm is faster even in the worst case when the optimal voltage vector is on the boundary. By further increasing the number of voltage levels in the case of the classic

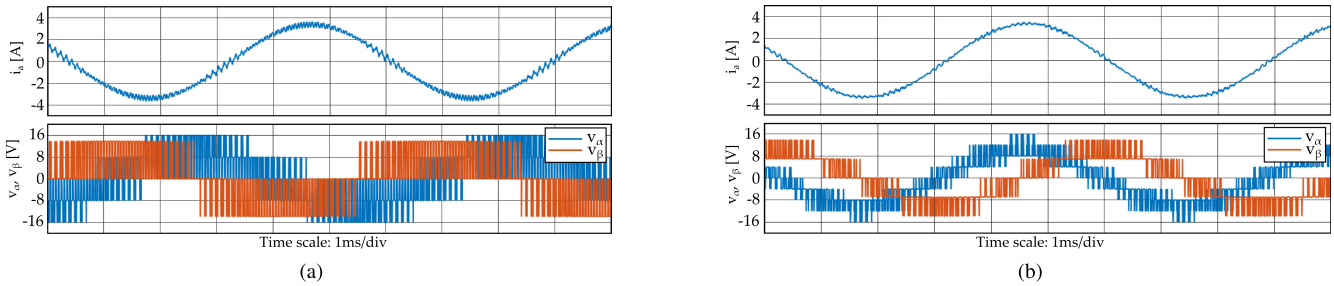

Fig. 11. Parameter sensitivity simulations. The operation is shown for nominal ($0-0.4$ s), 1.5 times nominal ($0.4-0.8$ s), and 0.5 times nominal values ($0.8-1.2$ s). Each phase starts unloaded, and then after 0.1 s passes, nominal load is applied, which lasts for 0.2 s, when it is removed. (a) Parameter sensitivity of R_s. (b) Parameter sensitivity of L_q.

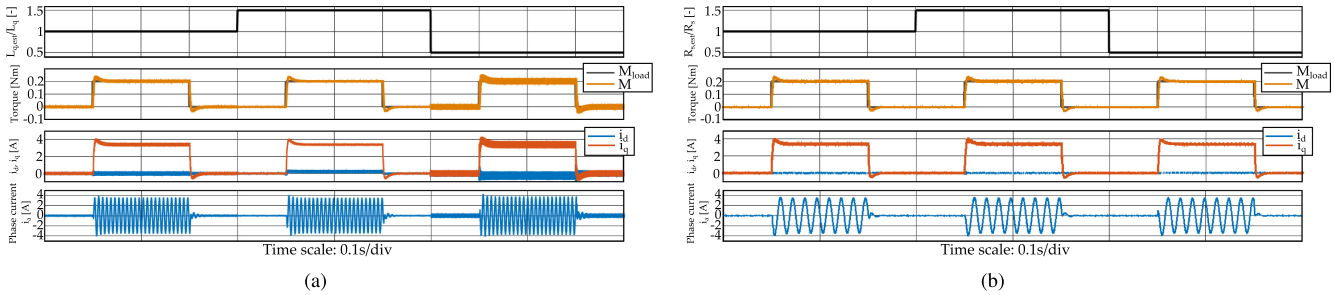

Fig. 12. Steady-state operation under nominal load for 2L- (left) and 3L-VSI (right) fed configurations. (a) 2L-VSI steady-state operation. (b) 3L-VSI steady-state operation.

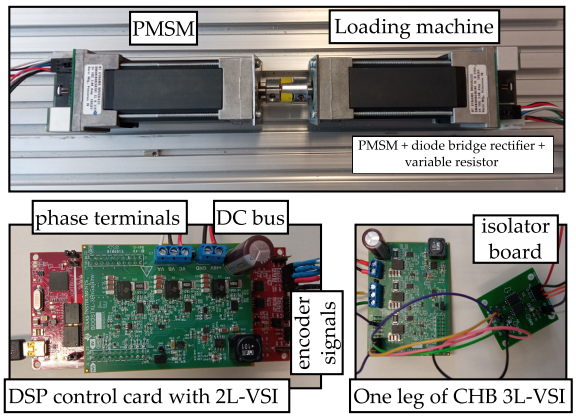

Fig. 13. Laboratory measurement setup.

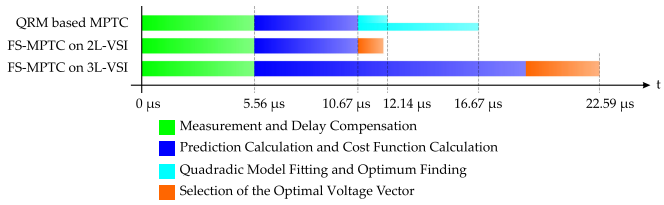

Fig. 14. Measured turnaround time of the required time for each of the tasks required by the QRM-MPC (upper) and FS-MPTC methods on two- (middle) and three-level (lower) VSIs on the utilized hardware.

MPTC scheme, the turnaround time increases as the predictions should be calculated for each of the applicable voltage vectors. However, the turnaround time for the QRM-MPC scheme will be the same as it is independent of the number of voltage levels. It is a clear advantage of the presented method, and therefore, it is a promising technique for ac drives supplied by ML-VSI as well.

It should be noted that the classic FS-MPTC schemes output the switching signals directly, while the QRM-MPC scheme generates only the optimal voltage vector at the end of the algorithm. The switching signals can be generated in the latter case by a proper PWM scheme. The duration of the PWM algorithm is not taken into account in Fig. 14 since this time depends on the complexity of the applied VSI topology and the used modulation method. In the presented experiments, the duration of the PWM algorithm added only a short extra time.

E. Experimental Results

The dynamic behavior of the QRM-MPC scheme using a 2L-VSI is demonstrated in Fig. 15, where Ω_{ref} is being set to -220 rad/s at 0.05 s. At 0.5 s, the reference speed is reversed. The i_d and i_q stator current components were generated by the built-in digital–analog converter of the utilized DSP, and they were measured, along with the phase currents and the mechanical speed, by a digital oscilloscope. In the figure, it can be observed that the phase currents are well constrained during the speeding periods. The mechanical speed followed its reference value and the fast tracking of the i_q current is also achieved. The path of the stator current vector at rated loading condition ($M_{\text{load}} =$

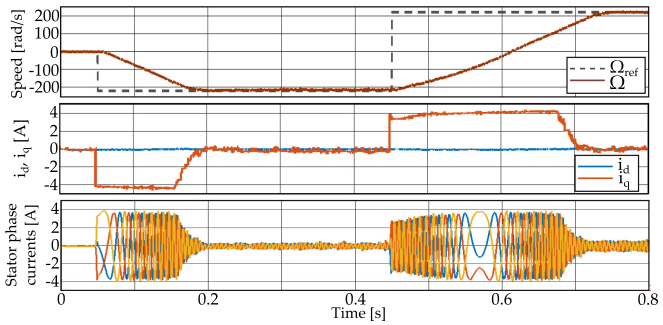

Fig. 15. Experimental results, step response of the method to changes in Ω_{ref}.

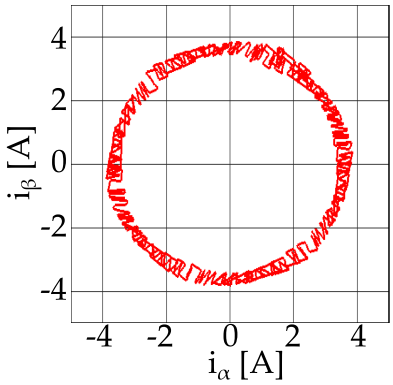

Fig. 16. Current vector trajectory in steady-state operation under nominal load and $\Omega_{\text{ref}} = 220$ rad/s.

$0.2\text{N} \cdot \text{m}$) at reference speed $\Omega_{\text{ref}} = 220$ rad/s can be seen in Fig. 16. The measured waveforms in Figs. 15 and 16 show a good resemblance with the simulation results presented in Figs. 9 and 10.

The QRM-MPC scheme was also tested using a three-level CHB inverter. The measured steady-state time function of the real component of the stator current vector, the real and imaginary component of the stator voltage vector in SRF, as well as the harmonic spectra of the current can be seen in Fig. 17(b). For better comparison, the same waveforms are measured and presented for 2L-VSI in Fig. 17(a). The figure demonstrates that the QRM-MPC scheme can work properly for ML-VSI as well. As it can be seen on the harmonic spectra of the current, the higher harmonics in the current signal can be found as sidebands around the f_s=10 kHz sampling (switching) frequency. The presented harmonic spectra are typical for electrical drives using PWM modulator [31]. As it can be seen, the amplitude of these sideband harmonics is slightly less for the 3L-VSI, which results in lower total harmonic distortion (THD) (5.6% for 2L-VSI versus 3.4% for 3L-VSI).

Fig. 18 presents the measured behavior of the drive for parameter sensitivity. The reference speed was selected to be 220 rd/s and the machine was loaded by its rated torque. Contrary to the simulation, here the q-axis inductance value L_q—or in other words, the L_q/L_d ratio—used by the QRM-MPC scheme during the predictions was changed abruptly in both directions by 50%. As it can be seen in the figure, the QRM approach works properly under even such high differences in the parameters. The amplitude of the phase current is practically the same; there is only a slight offset in the d-axis and q-axis current components. The small fluctuations in the speed signal were caused by the finite resolution of the encoder signals. It should be noted that the ripples in the phase currents can be seen with lower amplitudes in Fig. 18 compared to the steady-state performance presented in Fig. 17. This was caused by the larger time window for recording the signals by the digital oscilloscope, which resulted in a lower sampling time.

V. Comparison of the Proposed QRM Method With Other Techniques

The introduced indirect QRM scheme is a hybrid MPC algorithm in the sense that the prediction is carried out on finite voltage vectors, similarly to FS-MPC methods, but it uses a modulator stage similarly to CCS-MPC techniques. In this section, the proposed QRM scheme is compared with both some FS and CCS approaches available in the literature.

A. Comparison With FSMPC Approaches

In the case of FS-MPC techniques, the cost function is evaluated for all the achievable voltage vectors. The optimal voltage vector is selected based on which voltage vector has the smallest cost function value. As it was mentioned in Section I, these techniques generally operate at low and not constant switching frequencies. It can result in poor current harmonic performance, which increases the harmonic losses and can cause larger ripples in the electric torque as well.

Fig. 19 presents the measured steady-state time function of the real component of the stator current vector as well as its harmonic spectra for FS-MPTC by using a 2L-VSI and 3L-VSI. In the first case, the prediction and cost function evaluation [see (27)] was carried out for seven voltage vectors, while for the CHB-type, 3L-VSI for 19 voltage vectors. In both cases, after calculating the cost function values for all the possible voltage vectors, the voltage vector that minimizes the cost function was selected. The machine and the laboratory equipment were the same as in Section IV; the sampling frequency was selected to be $f_s = 1/T_s$ =10 kHz. By comparing the results obtained by the QRM-MPC approach (see Fig. 17) under the same operating conditions, it can be concluded that the latter one, thanks to the modulator, has better harmonic performance and lower THD both for 2 L and 3L-VSI. As it was mentioned in Section I, the traditional FS-MPC approach does not provide a constant switching frequency. The measured equivalent switching frequency per transistor was 2.6 kHz for 2L-VSI and 2.1 kHz for 3L-VSI. The QRM approach provides a constant switching frequency (f_s=10 kHz) at the same sampling frequency.

Moreover, it can be observed that the harmonics for FS-MPTC are not concentrated around the sampling or switching frequency and they spread over low-order harmonics.

By comparing the response of FS-MPTC using 2L-VSI and 3L-VSI, it can be concluded that the latter has better harmonic performance, but the turnaround time is larger as well (see

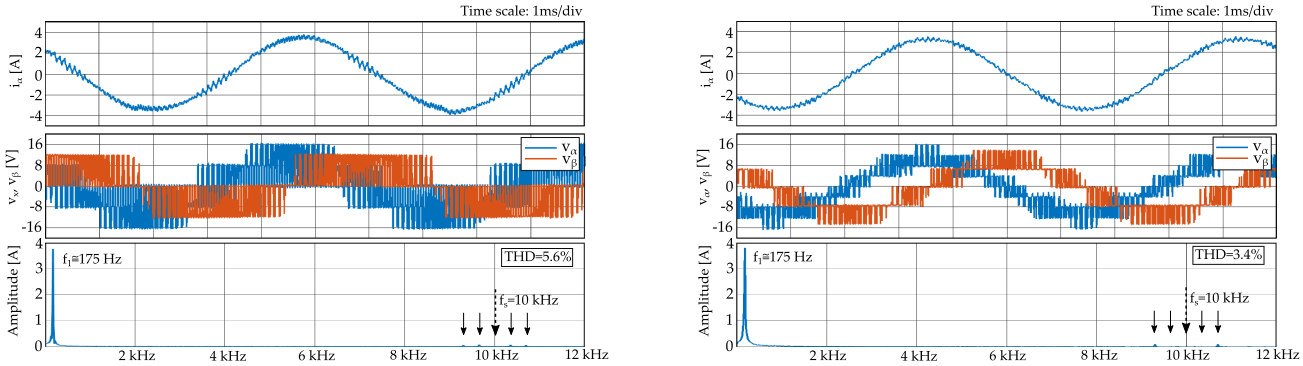

Fig. 17. Steady-state operation under nominal load for 2L- (left) and 3L-VSI (right) fed configurations. (a) 2L-VSI steady-state operation. (b) 3L-VSI steady-state operation.

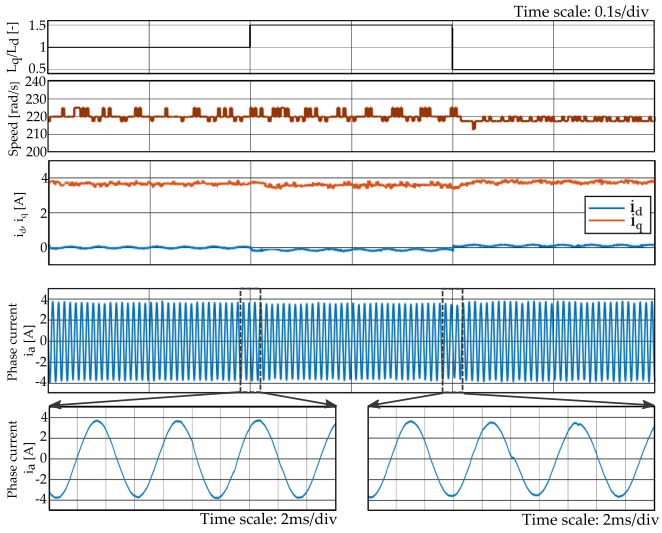

Fig. 18. Parameter sensitivity measurements. The $\frac{L_q}{L_d}$ ratio used in the prediction equations was changed abruptly in both directions by 50%.

Fig. 14) as the cost function should be evaluated for more voltage vectors.

It should be noted, as it was mentioned in Section I, that the performance of FS-MPC schemes can be improved [7]–[9], [11] with some modifications. In the measurement, the traditional direct FS-MPTC was assumed, where the controller outputs one voltage vector each sampling period.

It can be concluded that the proposed indirect QRM scheme has the clear advantage that the switching is deterministic and constrained by the dedicated modulator. It imposes a constant switching frequency, which results in better harmonic performance than the FS-MPC scheme at the same sampling frequency. The lower distortion in the current can cause lower torque ripples as well. Of course, the calculation of the quadratic model increases the computational load compared with classic FS-MPC techniques. However, as it was demonstrated in Section IV, the extra calculation time is not crucial for a 2L-VSI (see Fig. 14). Furthermore, the computational time of the QRM scheme does not depend on the number of voltage levels of the inverter. As it was demonstrated, the calculation time of FS-MPC, due to the increased number of predictions for the voltage vectors, can be larger for multilevel inverters than the total calculation time of the proposed technique.

B. Comparison With Continuous Set MPC Approaches

The proposed QRM method can be compared to indirect CCS-MPC techniques in many aspects. In most cases, these techniques apply a dedicated modulator stage. The switching frequency, the steady-state harmonic performance, and the magnitude of torque ripples are mainly determined by the used PWM technique and not the MPC algorithm itself. Therefore, the comparison of the QRM techniques with other schemes is compared in this section based on the required computational burden as this is a critical issue from the practical implementation point of view of MPC techniques.

In CCS-MPC techniques to find the optimal control action (voltage vector), the control problems are formulated as a QP problem. Thanks to the recent developments, the QP solvers enable real-time implementation even for embedded controllers. The two most widely used approaches in power electronics applications for QP solvers are the gradient methods and the active-set methods.

Yang *et al.* [25] present a gradient method for a direct MPC scheme. However, this technique does not apply a dedicated modulator; it can operate at a constant switching frequency. The method was demonstrated on a current-controlled induction machine drives by using a dSPACE SCALEXIO system, consisting of a 4 GHz Intel XEON processor and a Xilinx Kintex-7 FPGA. The required average iteration number was 39.7 (maximum 98), while the average time required for the algorithm was 16.9 μs (maximum 42.6 μs). Similar to this article, a low-cost DSP (TMS320F240) was used in [26], which demonstrates a fast gradient method to solve a constrained finite-time optimal control problem to select the voltage vector for a PMSM drive. In this article, the turnaround time is limited to 70 μs to maintain a constant 10 kHz sampling frequency, which is the same as in our

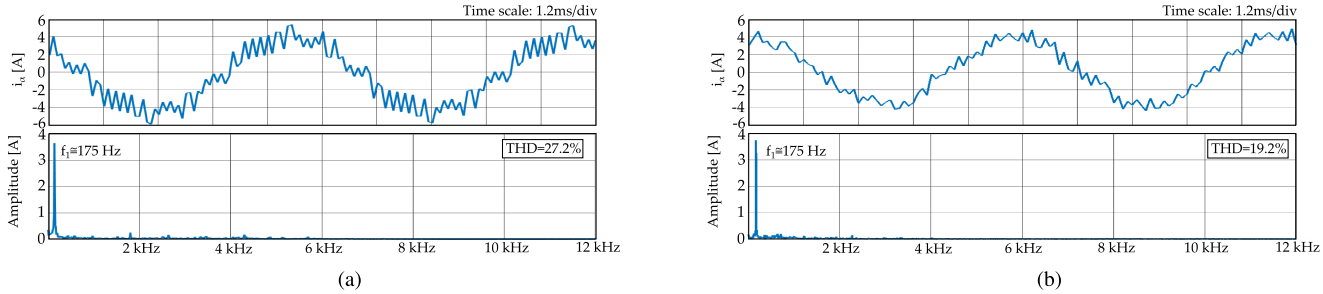

Fig. 19. Steady-state operation under nominal load for 2L- (left) and 3L-VSI (right) fed configurations. (a) FS-MPC 2L-VSI steady-state operation. (b) FS-MPC 3L-VSI steady-state operation.

case. It results that for a single prediction horizon, the maximum number of iterations was restricted to eight.

A gradient-based method with a fixed number of iterations by using a Lagrangian approach is introduced in [16]. The method was demonstrated on a PMSM drive by using a dSPACE DS1202 real-time platform. The achieved sampling frequency of the method was 2 kHz.

An active-set algorithm for solving the QP problem for MPTC-controlled PMSM was demonstrated in [17]. For the worst-case scenario, the total number of arithmetic operations for the solver was 2431 among them 10 square roots. The method was implemented on similar hardware (TMS320F28335) that is being used in this article. The achieved sampling time was 0.3 ms. The calculation time for the MPC approach is not constant; it fluctuates between 0.15 and 0.25 ms having a variable number of iterations between 2 and 6.

In the literature, many articles use the so-called qpOASES open-source software package, which implements a parametric active-set reliably and efficiently [33]. A great advantage of the package is that it provides an interface for Simulink, which can allow to directly compile the algorithm to dSPACE or xPC target hardware. Due to the generality of this solver, the computational load is relatively high. In [33], 6 kHz sampling frequency could be reached by using a high-performance dSPACE system. Hanke *et al.* [34] applied also the qpOASES solver for the MPC control of a PMSMS by using a dSPACE DS1006MC system. The algorithm used three cores for solving the optimization problem, while a fourth core was used to process the measurements and precalculate the matrices and vectors. The resulting computational time of the MPC scheme on the multicore hardware was measured between 10 and 26 μs with an average of 15 μs.

Favato *et al.* [35] propose a computation-efficient solver for QP problems. The scheme was elaborated on the current control of a synchronous machine. The method was compared for different cases with qpOASES and it was turned out that the computational time can be reduced circa 20 times. The QP solver method—without the prediction and the cost function calculation—in the worst-case scenario uses 102 multiplications, 82 additions, and 6 divisions. The method is implemented on a dSPACE MicroLabBox, which is a dual-core real-time processor operating at 2 GHz. The measured average turnaround time only of the algorithm was 12 μs.

By comparing the performance of the proposed indirect QRM scheme with the techniques presented above, it can be concluded that the QRM scheme has a great advantage in that it is not an iterative method. Therefore, the total number of operations can be determined, the maximum computational time is known *a priori*, contrary to the methods presented in [17], [25], [26], and [35]. As it was mentioned in the previous sections, the QRM scheme—without the measurement and delay compensation—needs 131 multiplications, 92 additions/subtractions, and 1 division if $\mathbf{H}_m \succ 0$ and the respective minimum is inside the boundary constraints. During the implementation, the turnaround time on a low-cost DSP was only 6.58 μs (see Fig. 14) for this case without the measurement and delay compensation. If the $\mathbf{H}_m \succ 0$ and the voltage constraints are violated, the optimum should search on the boundary segments. In this case, the total number of operations increases to 234 multiplications, 144 additions/subtractions, and 4 divisions, while the measured turnaround time on the DSP is increased to 11.11 μs. As it can be seen, the presented method has to execute far fewer arithmetic operations as presented in [17] and is very similar to those reported in [35]. By comparing the number of arithmetic operations with the method presented in [35], it can be concluded that they perform very similarly. The number of arithmetic operations for the worst case for [35] was given only for solving the QP problem without the cost function evaluation. In the proposed QRM scheme, a QP problem is solved in *Steps 3* and *4*. In the worst-case scenario (see Table I), the required number of multiplication is slightly greater than the method presented in [35] (122 versus 102), but the proposed scheme requires marginally less addition (74 versus 82) and divisions (4 versus 6).

The comparison of the measured turnaround times is generally not fair as it highly depends on the applied hardware. However, in most cases, the proposed QRM scheme has a shorter (or in the case of [35], very similar) computational time even on a low-cost DSP operating on a single-core than other techniques, which use much more powerful platforms.

One drawback of the presented QRM method is that it can work only for single-step prediction. By using a longer prediction horizon, the transient performance can be improved [2], [25], [35]. Furthermore, while some CCS techniques, such as [34], can operate on multicore hardware to obtain shorter calculation times, the QRM scheme can run only on a single

thread. At most, only the prediction step can be parallelized, but due to the low number of voltage vectors, it is not worth doing it. These results with the proposed QRM scheme generality of the considered solver increase the required time to solve the problem. However, even with such high-performance hardware, the achievable sampling frequency, due to the complexity of the algorithm, is limited.

VI. Conclusion

In this article, the indirect QRM-MPC approach was presented. The method proposes an alternative formulation of the QP problem that is at the core of indirect MPC schemes and allows a simple and effective solution. First, the cost function values are established as in FS-MPC schemes for seven voltage vectors. Then, a quadratic regression model specifically tailored for this purpose is being fit upon these results to continuously map the cost function upon the modulation region. The resulting optimization problem can be solved simply and efficiently since the complexity presented algorithm does not scale with the voltage levels of the utilized inverter. Furthermore, due to the formulation of the quadratic regression model, the calculations do not require complicated operations, such as square roots or exponentiation. Furthermore, the total number of operations is also known *a priori* for all possible cases, contrary to the widely used iterative methods used in the literature. Therefore, the turnabout time of the method can be estimated for any given hardware.

The indirect QRM-MPC approach is demonstrated for a PMSM as a case study, with both simulation and experimental results presented comparatively. To increase the precision of the discrete model, the equations of the PMSM were established using the Tustin transformation. As it was demonstrated, the proposed scheme can find the optimal voltage vector in a few microseconds, making it promising for implementation in large-scale real-time industrial applications.

Appendix A
Boundary Optimum Finding Equations

The optimum on a given boundary segment can be determined via expressing v_y from the h_i equality constraint. Thus, from the regression model $m(v_x, v_y, \boldsymbol{\mu})$, the $m_i(v_x, \boldsymbol{\mu})$ is obtained.

$$\begin{aligned}
m_1(v_x,\boldsymbol{\mu}) &= av_x^2 + bv_x + \Big(3c(v_x-1) - \sqrt{3}(d+ev_x)\Big)\\
&\quad (v_x-1) + f\\
m_2(v_x,\boldsymbol{\mu}) &= av_x^2 + \left(b + \frac{\sqrt{3}}{2}e\right)v_x + \frac{3}{4}c + \frac{\sqrt{3}}{2}d + f\\
m_3(v_x,\boldsymbol{\mu}) &= av_x^2 + bv_x + \Big(3c(v_x+1) + \sqrt{3}(d+ev_x)\Big)\\
&\quad (v_x+1) + f\\
m_4(v_x,\boldsymbol{\mu}) &= av_x^2 + bv_x + \Big(3c(v_x+1) - \sqrt{3}(d+ev_x)\Big)\\
&\quad (v_x+1) + f\\
m_5(v_x,\boldsymbol{\mu}) &= av_x^2 + \left(b - \frac{\sqrt{3}}{2}e\right)v_x + \frac{3}{4}c - \frac{\sqrt{3}}{2}d + f\\
m_6(v_x,\boldsymbol{\mu}) &= av_x^2 + bv_x + \Big(3c(v_x-1) + \sqrt{3}(d+ev_x)\Big)\\
&\quad (v_x-1) + f.
\end{aligned} \tag{28}$$

The optimization process requires information about the first and second derivatives of m_i with respect to v_x. The critical point to each of the boundaries can be found via solving the $\frac{\partial m_i(v_x,\boldsymbol{\mu})}{\partial v_x} = 0$ equations. These equations are linear due to the properties of the functions listed in (28). Therefore, the critical point of a boundary segment can be expressed as a function of the regression model coefficients $\boldsymbol{\mu}$.

$$\begin{aligned}
v_{x,1,\text{crit}}(\boldsymbol{\mu}) &= -\frac{b - 6c + \sqrt{3}(e-d)}{2(a + 3c - \sqrt{3}e)}\\
v_{x,2,\text{crit}}(\boldsymbol{\mu}) &= -\frac{2b + \sqrt{3}}{4a}\\
v_{x,3,\text{crit}}(\boldsymbol{\mu}) &= -\frac{b + 6c + \sqrt{3}(d+e)}{2(a + 3c - \sqrt{3}e)}\\
v_{x,4,\text{crit}}(\boldsymbol{\mu}) &= -\frac{b + 6c - \sqrt{3}(d+e)}{2(a + 3c - \sqrt{3}e)}\\
v_{x,5,\text{crit}}(\boldsymbol{\mu}) &= -\frac{2b - \sqrt{3}}{4a}\\
v_{x,6,\text{crit}}(\boldsymbol{\mu}) &= -\frac{b - 6c + \sqrt{3}(d-e)}{2(a + 3c - \sqrt{3}e)}.
\end{aligned} \tag{29}$$

The calculated critical points can either be maxima or minima, depending on the value of the second derivative of m_i with respect to v_x at the point of the optimum. However, the second derivatives are constants due to the original function being a second-degree polynomial. The second derivatives of m_i can also be calculated since the optimization problem is the same for all sampling instants, only the coefficients of the regression model change. The second derivatives are, thus, the following:

$$\begin{aligned}
\frac{\partial^2 m_1(v_x,\boldsymbol{\mu})}{\partial v_x^2} &= \frac{\partial^2 m_4(v_x,\boldsymbol{\mu})}{\partial v_x^2} = 2a + 6c - 2\sqrt{3}e\\
\frac{\partial^2 m_2(v_x,\boldsymbol{\mu})}{\partial v_x^2} &= \frac{\partial^2 m_5(v_x,\boldsymbol{\mu})}{\partial v_x^2} = 2a\\
\frac{\partial^2 m_3(v_x,\boldsymbol{\mu})}{\partial v_x^2} &= \frac{\partial^2 m_6(v_x,\boldsymbol{\mu})}{\partial v_x^2} = 2a + 6c + 2\sqrt{3}e.
\end{aligned} \tag{30}$$

It is important to note that the denominators in (29) are the same expressions to the respective m_i as (30).

Appendix B
Coefficient of Determination

A well-established goodness-of-fit measure of linear regression models is the R-squared value. It is defined as the following in [36]:

$$R^2 = 1 - \frac{\text{SS}_{\text{residual}}}{\text{SS}_{\text{total}}} \tag{31}$$

$$\mathrm{SS}_{\mathrm{total}} = \sum_{i=1}^{n} (g(\mathbf{v}_i) - \overline{g})^2 \tag{32}$$

$$\overline{g} = \frac{1}{n} \sum_{i=1}^{n} g(\mathbf{v}_i) \tag{33}$$

$$\mathrm{SS}_{\mathrm{residual}} = \sum_{i=1}^{n} (m(v_{i,x}, v_{i,y}, \boldsymbol{\mu}) - g(\mathbf{v}_i))^2 \tag{34}$$

where $\mathrm{SS}_{\mathrm{total}}$ is the total sum of squares, $\mathrm{SS}_{\mathrm{residual}}$ is the residual sum of squares, and $\overline{g}$ is the mean of the observed cost function data for the voltage vectors. As there were six predictors used in this work, the mention of the adjusted R-squared ($\overline{R}^2$) value is warranted

$$\overline{R}^2 = 1 - (1 - R^2) \frac{n-1}{n-k-1} \tag{35}$$

where k is the number of model parameters (excluding the constant term). This method penalizes models that utilize many variables to describe the process.

Appendix C
Calculating the Optimal Voltage Vector for a Given Working Point

In this section, the calculation of the optimal voltage vector is presented for a given set of measurement data. The presented calculations use the motor parameters given in II. The V_{DC} bus voltage was set to 24 V in correspondence with the simulations and measurements.

The controller requires the measurement of two-phase currents to establish the actual current vector in the $\alpha - \beta$ SRF. Furthermore, the speed of the machine and the mechanical angle are measured. In the given working point, these are

$i_a(kT_s) = -2.9638$ A $\quad i_b(kT_s) = 0.2842$ A

$\alpha_m(kT_s) = 0.4016$ rad $\quad \Omega(kT_s) = 220.0$ rad/s.

The measurement data are processed to obtain the current in the $\alpha - \beta$ SRF. The electrical angle and angular velocity are also calculated from the number of pole pairs.

$i_\alpha(kT_s) = -2.9638$ A $\quad i_\beta(kT_s) = -1.3830$ A

$\alpha_e(kT_s) = 2.0079$ rad $\quad \omega_1(kT_s) = 1100.00$ rad/s.

From the electrical angle, the transformation matrix $\mathbf{R}(\alpha_e)$ can be calculated that transforms a vector in the $\alpha\beta$ SRF to the dq RRF

$$\mathbf{R}(\alpha_e) = \begin{bmatrix} -0.4233 & -0.9060 \\ 0.9060 & -0.4233 \end{bmatrix}.$$

The current is transformed to the dq coordinate system: $[i_d, i_q]^{\mathrm{T}} = \mathbf{R}(\alpha_e)[i_\alpha, i_\beta]^{\mathrm{T}}$

$i_d(kT_s) = 0.0017$ A $\quad i_q(kT_s) = 3.2707$ A.

Using (8), the parameters for the current prediction can be established

$\gamma = 19979.83,\ A = 0.9147,\ B = 0.0527,\ C = -0.0527$

$D = 0.9147,\ E = -329.41,\ F = 0.2995,\ G = 0.2995.$

The current is to be compensated for the delay. However, in order to establish this prediction, the optimal voltage vector calculated for the previous sample is required. This voltage vector is being modulated in the $[kT_s, kT_s + T_s]$ interval. It is available in the xy normalized form

$v_x(kT_s) = -0.5180 \quad v_y(kT_s) = -0.3218.$

The previous voltage vector is now transformed back to the $\alpha\beta$ and then to the dq reference frames, respectively.

$$[v_\alpha, v_\beta]^{\mathrm{T}} = \frac{3}{2} V_{\mathrm{DC}} [v_x, v_y]^{\mathrm{T}}$$

$$v_\alpha(kT_s) = -8.2878 \text{ V} \quad v_\beta(kT_s) = -5.1481 \text{ V}$$

$$[v_d, v_q]^{\mathrm{T}} = \mathbf{R}(\alpha_e)[v_\alpha, v_\beta]^{\mathrm{T}}$$

$$v_d(kT_s) = -1.1552 \text{ V} \quad v_q(kT_s) = 9.6879 \text{ V}$$

The delay and then the predictions for the voltage vectors of the inverter can be calculated as (9)

$$\begin{aligned} \begin{bmatrix} i_d \\ i_q \end{bmatrix} (kT_s + T_s) = & \begin{bmatrix} 0.9093 & 0.1006 \\ -0.1006 & 0.9093 \end{bmatrix} \begin{bmatrix} i_d \\ i_q \end{bmatrix} (kT_s) \\ & + \begin{bmatrix} 0.2986 & 0.0157 \\ -0.0157 & 0.2986 \end{bmatrix} \begin{bmatrix} v_d \\ v_q \end{bmatrix} (kT_s) \\ & + \begin{bmatrix} -17.3139 \\ -328.501 \end{bmatrix} \Psi_{\mathrm{PM}}. \end{aligned} \tag{36}$$

The delay compensated current assumes the following values:

$i_d(kT_s + T_s) = 0.0015$ A $\quad i_q(kT_s + T_s) = 3.2902$ A.

Using $i_d(kT_s + T_s)$ and $i_q(kT_s + T_s)$ and the voltage vectors of the inverter in the dq coordinate systems, the predictions for the $i_d(kT_s + 2T_s)$ and $i_q(kT_s + 2T_s)$ can be obtained using (9) with the respective voltage vectors (see fourth and fif th column of Table III). The predictions were done for all of the voltage vectors of a 2L-VSI. The results are summarized in Table III. The table includes the associated cost function values for each of the voltage vectors using (27), with the torque reference being $M_{\mathrm{ref}} = 0.1866$ N· m, for the seven voltage vectors ($\mathbf{v}_1, \ldots, \mathbf{v}_7$) required for the QRM approach (see rows i=[1,7] of the sixth column of Table C1).

Using the first seven cost function values, the quadratic regression model coefficients can be determined using (18)

$$\begin{bmatrix} a \\ b \\ c \\ d \\ e \\ f \end{bmatrix} = \frac{1}{6} \begin{bmatrix} 3 & 0 & 0 & 3 & 0 & 0 & -6 \\ 2 & 1 & -1 & -2 & -1 & 1 & 0 \\ -1 & 2 & 2 & -1 & 2 & 2 & -6 \\ 0 & \sqrt{3} & \sqrt{3} & 0 & -\sqrt{3} & -\sqrt{3} & 0 \\ 0 & 2\sqrt{3} & -2\sqrt{3} & 0 & 2\sqrt{3} & -2\sqrt{3} & 0 \\ 0 & 0 & 0 & 0 & 0 & 0 & 6 \end{bmatrix} \begin{bmatrix} 4.3954 \\ 7.5980 \\ 24.8015 \\ 5.9939 \\ 5.4601 \\ 21.0652 \\ 0.0649 \end{bmatrix} \tag{37}$$

which results $\boldsymbol{\mu} = [a, b, c, d, e, f]^{\mathrm{T}} = [5.1297,\ -0.7992,\ 17.8452,\ 1.6957,\ -18.9420,\ 0.0649]^{\mathrm{T}}$.

The determination of the optimal voltage vector begins with the calculation whether the Hessian is positive definite. Since $a = 5.1297 > 0$ and $4ac - e^2 = 7.3604 > 0$, the $\mathbf{H}_m \succ 0$ is implied. Therefore, the optimal voltage vector can be determined

using (23) as

$$\mathbf{v}_{\text{crit}} = \frac{1}{4ac - e^2} \begin{bmatrix} de - 2bc \\ be - 2ad \end{bmatrix} = \begin{bmatrix} -0.4885 \\ -0.3068 \end{bmatrix}. \quad (38)$$

Since $\mathbf{v}_{\text{crit}}$ does not violate any of the constraints, it can be accepted as the optimal control action. Therefore, $\mathbf{v}_{\text{opt}} = \mathbf{v}_{\text{crit}}$ is forwarded to the modulator as a voltage vector reference.

To demonstrate that, the developed continuous quadratic regression model perfectly maps the cost function upon the entire modulation region and the scheme can be used for ML-VSI as well; the cost function is evaluated for the additional 12 voltage vectors for a 3L-VSI and the values are compared with the cost function values calculated from the regression model. The second part of Table C1 (see rows i=[8,19]) presents the calculation results for these additional voltage vectors. The first column gives the number of voltage vectors [for the numbering, see Fig. 2(b)], while the second and third columns present the x and y components of the voltage vectors. The result of the current predictions [see (9)] can be found in the fourth and fifth columns. The sixth column $g(\mathbf{v}_i)$ gives the value of the cost function (assuming unity weighting factor) calculated from (27). The seventh column $m(v_{i,x}, v_{i,y}, \boldsymbol{\mu})$ gives the value of the cost function calculated by using the regression model using (11). The last column presents the square of the residual, which is calculated as $(g(\mathbf{v}_i) - m(v_{i,x}, v_{i,y}, \boldsymbol{\mu}))^2$.

Based on the results represented in Table C1, it can be concluded that even though the quadratic regression model function was established by seven cost function predictions, it can evaluate the cost function perfectly for the other voltage vectors as well. The coefficient of determination can be calculated as (31) with the following results for the total sum of squares and the residual sum of squares: $\text{SS}_{\text{residual}} = 1.8230\text{e-}28 \quad \text{SS}_{\text{total}} = 941.92$

$$R^2 = 1 - \frac{\text{SS}_{\text{residual}}}{\text{SS}_{\text{total}}} = 1 - 1.9355\text{e-}31. \quad (39)$$

Since the coefficient of determination is practically 1, the authors conclude that the quadratic regression model function can perfectly extend the cost function upon the modulation region.

REFERENCES

[1] P. Karamanakos, E. Liegmann, T. Geyer, and R. Kennel, "Model predictive control of power electronic systems: Methods, results, and challenges," *IEEE Open J. Ind. Appl.*, vol. 1, pp. 95–114, Aug. 2020.

[2] P. Karamanakos and T. Geyer, "Guidelines for the design of finite control set model predictive controllers," *IEEE Trans. Power Electron.*, vol. 35, no. 7, pp. 7434–7450, Jul. 2020.

[3] J. Rodriguez *et al.*, "Latest advances of model predictive control in electrical drives—part I: Basic concepts and advanced strategies," *IEEE Trans. Power Electron.*, vol. 37, no. 4, pp. 3927–3942, Apr. 2022.

[4] J. Rodriguez *et al.*, "Latest advances of model predictive control in electrical drives. Part II: Applications and benchmarking with classical control methods," *IEEE Trans. Power Electron.*, vol. 37, no. 5, pp. 5047–5061, May 2022.

[5] M. F. Elmorshedy, W. Xu, F. F. M. El-Sousy, M. R. Islam, and A. A. Ahmed, "Recent achievements in model predictive control techniques for industrial motor: A comprehensive state-of-the-art," *IEEE Access*, vol. 9, pp. 58170–58191, 2021.

[6] R. Jose and C. Patricio, *Predictive Control of Permanent Magnet Synchronous Motors*. Hoboken, NJ, USA: Wiley, 2012, ch. 9, pp. 133–144. [Online]. Available:https://onlinelibrary.wiley.com/doi/abs/

[7] C. Xue, L. Ding, H. Tian, and Y. Li, "Multi-rate finite-control-set model predictive control for high switching frequency power converters," *IEEE Trans. Ind. Electron.*, vol. 69, no. 4, pp. 3382–3392, Apr. 2022.

[8] X. Zhang and B. Hou, "Double vectors model predictive torque control without weighting factor based on voltage tracking error," *IEEE Trans. Power Electron.*, vol. 33, no. 3, pp. 2368–2380, Mar. 2018.

[9] Y. Luo and C. Liu, "Multi-vector-based model predictive torque control for a six-phase PMSM motor with fixed switching frequency," *IEEE Trans. Energy Convers.*, vol. 34, no. 3, pp. 1369–1379, Sep. 2019.

[10] Y. Zhang, D. Xu, and L. Huang, "Generalized multiple-vector-based model predictive control for PMSM drives," *IEEE Trans. Ind. Electron.*, vol. 65, no. 12, pp. 9356–9366, Dec. 2018.

[11] J. Qu, J. Jatskevich, C. Zhang, and S. Zhang, "Improved multiple vector model predictive torque control of permanent magnet synchronous motor for reducing torque ripple," *IET Electric Power Appl.*, vol. 15, no. 6, pp. 681–695, Jun. 2021.

[12] X. Wang and D. Sun, "Three-vector-based low-complexity model predictive direct power control strategy for doubly fed induction generators," *IEEE Trans. Power Electron.*, vol. 32, no. 1, pp. 773–782, Jan. 2017.

[13] Y. Yang *et al.*, "Low complexity finite-control-set MPC based on discrete discrete space vector modulation for T-type three-phase three-level converters," *IEEE Trans. Power Electron.*, vol. 37, no. 1, pp. 392–403, Jan. 2022.

[14] S. Niu, Y. Luo, W. Fu, and X. Zhang, "An indirect reference vector-based model predictive control for a three-phase PMSM motor," *IEEE Access*, vol. 8, pp. 29435–29445, 2020.

[15] S. Yuntao, X. Xiang, Z. Yuan, Z. Hengjie, and S. Dehui, "Design of explicit model predictive control for PMSM drive systems," in *Proc. 29th Chin. Control And Decis. Conf.*, 2017, pp. 7389–7395.

[16] T. Englert and K. Graichen, "A fixed-point iteration scheme for model predictive torque control of PMSMS," *IFAC-PapersOnLine*, vol. 51, pp. 568–573, 2018.

[17] G. Cimini, D. Bernardini, S. Levijoki, and A. Bemporad, "Embedded model predictive control with certified real-time optimization for synchronous motors," *IEEE Trans. Control Syst. Technol.*, vol. 29, no. 2, pp. 893–900, Mar. 2021.

[18] F. Toso, P. G. Carlet, A. Favato, and S. Bolognani, "On-line continuous control set MPC for PMSM drives current loops at high sampling rate using qpOASES," in *Proc. IEEE Energy Convers. Congr. Expo.*, 2019, pp. 6615–6620.

[19] A. A. Ahmed, B. K. Koh, and Y. I. Lee, "A comparison of finite control set and continuous control set model predictive control schemes for speed control of induction motors," *IEEE Trans. Ind. Inform.*, vol. 14, no. 4, pp. 1334–1346, Apr. 2018.

[20] Y. Li, P. Zhang, J. Hang, S. Ding, L. Liu, and Q. Wang, "Comparison of dynamic characteristics of field oriented control and model predictive control for permanent magnet synchronous motor," in *Proc. 13th IEEE Conf. Ind. Electron. Appl.*, 2018, pp. 2431–2434.

[21] A. V. Oppenheim and R. W. Schafer, *Discrete-Time Signal Processing*, 3rd ed. Englewood Cliffs, NJ, USA: Prentice-Hall, 2009.

[22] S. Vazquez, J. Rodriguez, M. Rivera, L. G. Franquelo, and M. Norambuena, "Model predictive control for power converters and drives: Advances and trends," *IEEE Trans. Ind. Electron.*, vol. 64, no. 2, pp. 935–947, Feb. 2017.

[23] C. Egert, *Lineare Statistische Modellierung und Interpretation in der Praxis*. Munich, Germany: Oldenbourg Wissenschaftsverlag, 2012. [Online]. Available: https://doi.org/10.1524/9783486723809

[24] L. Halbeisen, N. Hungerbühler, S. Schumacher, and G. X. Yau, "Sets of range uniqueness for multivariate polynomials and linear functions with rank k," *Linear Multilinear Algebra*, vol. 1, pp. 1–19, 2021. [Online]. Available: https://doi.org/10.1080/03081087.2021.1922338

[25] Q. Yang *et al.*, "Computationally efficient fixed switching frequency direct model predictive control," *IEEE Trans. Power Electron.*, vol. 37, no. 3, pp. 2761–2777, Mar. 2022.

[26] M. Preindl, S. Bolognani, and C. Danielson, "Model predictive torque control with PWM using fast gradient method," in *Proc. 28th Annu. IEEE Appl. Power Electron. Conf. Expo.*, 2013, pp. 2590–2597.

[27] B. Wilamowski and J. Irwin, *Power Electronics and Motor Drives* (Electrical Engineering Handbook series). Boca Raton, FL, USA: CRC Press, 2018. [Online]. Available: https://doi.org/10.1201/9781315218410

[28] G. Narayanan and V. T. Ranganathan, "Extension of operation of space vector PWM strategies with low switching frequencies using different overmodulation algorithms," *IEEE Trans. Power Electron.*, vol. 17, no. 5, pp. 788–798, Sep. 2002.

[29] E.-S. Jun, M. H. Nguyen, and S.-S. Kwak, "Model predictive control method with np voltage balance by offset voltage injection for three-phase

[30] V. Jayakumar, B. Chokkalingam, and J. L. Munda, "A comprehensive review on space vector modulation techniques for neutral point clamped multi-level inverters," *IEEE Access*, vol. 9, pp. 112104–112144, 2021.
[31] D. G. Holmes and T. A. Lipo, *Pulse Width Modulation for Power Converters: Principles and Practice*, vol. 18. Hoboken, NJ, USA: Wiley, 2003.
[32] M. Preindl and S. Bolognani, "Model predictive direct torque control with finite control set for PMSM drive systems, part 1: Maximum torque per ampere operation," *IEEE Trans. Ind. Inform.*, vol. 9, no. 4, pp. 1912–1921, Nov. 2013.
[33] H. J. Ferreau, C. Kirches, A. Potschka, H. G. Bock, and M. Diehl, "qpOASES: A parametric active-set algorithm for quadratic programming," *Math. Program. Comput.*, vol. 6, no. 4, pp. 327–363, 2014. [Online]. Available: https://doi.org/10.1007/s12532-014-0071-1
[34] S. Hanke, O. Wallscheid, and J. Böcker, "Continuous-control-set model predictive control with integrated modulator in permanent magnet synchronous motor applications," in *Proc. IEEE Int. Electr. Mach. Drives Conf.*, 2019, pp. 2210–2216.
[35] A. Favato *et al.*, "Efficient QP solver for electric motors," Aug. 2021. [Online]. Available: https://www.techrxiv.org/articles/preprint/Fast_Solver_for_Implicit_Continuous_Set_Model_Predictive_Control_of_Electric_Drives/15067401/3
[36] J. Miles, *R Squared, Adjusted R Squared*. American Cancer Society, 2014. [Online]. Available: https://onlinelibrary.wiley.com/doi/abs/10.1002/9781118445112.stat06627

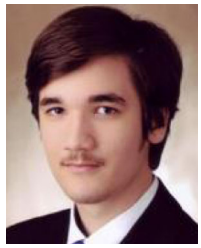

Kristóf Bándy was born in Budapest, Hungary, in 1995. He received the M.S. degree in mechatronics engineering in 2021 from the Budapest University of Technology and Economics, Budapest, Hungary, where, since 2021, he has been working toward the Ph.D. degree in electrical engineering with the Department of Automation and Applied Informatics, Faculty of Electrical Engineering and Informatics.

His current research interests include model predictive control of electric drives, power electronics, and machine learning.

Péter Stumpf was born in Budapest, Hungary, in 1985. He received the M.S. and Ph.D. degrees in mechanical engineering from the Budapest University of Technology and Economics, Budapest, Hungary, in 2009 and 2014, respectively.

From 2013 and 2019, he was a Senior Lecturer with the Department of Automation and Applied Informatics, Faculty of Electrical Engineering and Informatics, Budapest University of Technology and Economics. Since 2019, he has been an Associate Professor. His current research interests interests include high-speed electrical drives, power electronics, and variable structure nonlinear systems.